Progress In Electromagnetics Research B, Vol. 82, 49–71, 2018

Extraordinary Transmission through Subwavelength Hole Arrays for General Oblique Incidence — Mechanism as Related to Surface Wave Dispersion and Floquet Lattice Diagrams

Malcolm Ng Mou Kehn*

Abstract—An array of rectangular holes pierced through a conducting screen is treated herein by a rigorous full-wave modal analysis using the moment method entailing Green's functions for rectangular cavities and planar multilayer structures in the spectral domain. Unexpectedly strong diffusions of incident plane waves are observed even at frequencies where the size of each hole is considerably less than the wavelength, posing a transmission efficiency that exceeds unity and thus leading to extraordinary transmission since this defies classical aperture diffraction theory. This paper fortifies the present understanding of the role surface plasmon polaritons (SPP) play in explaining this phenomenon, by using surface-wave dispersion and Floquet lattice diagrams to link up with the peaks in the transmission spectra. The incidence angle and polarization of the irradiation are taken into account in this work.

1. INTRODUCTION

As early as the 1960s, there had already been works reporting measured transmission resonances through metal grids [1–3], meshes [3, 4], and circular hole arrays [5, 6]. There were however still no inkling then about anything peculiar with these surges in wave diffusion. Rather, initial studies of this phenomenon were essentially hinged on their filtering capabilities that spurred applications in antennas, frequency-selective surfaces, and artificial dielectrics [7]. It was not until 1998 when Ebbesen et al. experimentally demonstrated extraordinary transmission (ET) of light through a metallic film perforated by an array of subwavelength holes [8] using focused-ion beam milling; extraordinary being in the sense that the transmission can be orders of magnitude larger than expected from classical aperture theory [9]. This seminal work triggered an outburst of research into the optical properties and transmission characteristics of hole-arrays throughout the electromagnetic spectrum. Indexed citations to Ebbesen's original paper have reached the scale of thousands, and the activities show no signs of slowing down.

Aside from its fundamental scientific interest, extraordinary transmission through subwavelength hole arrays along with its light confinement capabilities has an eclectic range of applications, such as subwavelength photolithography, near-field microscopy, wavelength-tunable filters, optical modulators, filters, and polarizers, nonlinear optics, sensing and spectroscopy, quantum optics, and subwavelength imaging [10–12], encompassing even the far reaches of cutting edge technology such as the tracking and detection of single molecule fluorescence in biology and chemistry, ultrafast photodetectors for optoelectronics, vibrational spectroscopy of molecular monolayers, and fluorescence correlation spectroscopy [13–16].

Surface plasmon polaritons (SPP) [17] are oscillatory excitations of collective electron densities on the surface of a metal. Generated by the periodically textured conducting surface that results from an

Received 5 July 2018, Accepted 13 September 2018, Scheduled 27 September 2018

* Corresponding author: Malcolm Ng Mou Kehn (malcolmaxwell@gmail.com).
The author is with the Department of Electrical and Computer Engineering, Institute of Communications Engineering, as well as the Center for mmWave Smart Radar Systems and Technologies at the National Chiao Tung University, Hsinchu, Taiwan.

array of holes pierced into a metallic screen, the role of SPP in the enhancement of wave penetration has been postulated [8, 18–22]. Plasmon excitations at interfaces on both sides of the screen are believed to occur due also to a channel [23, 24] provided by the periodic holes, which couple them to each other [25–27]. The incident radiation interacts with these surface plasmons, leading to ET of waves. In [28], the role played by guided modes within the hole was also demonstrated.

Fabry-Perot cavity resonances are standing waves that are established between two parallel reflecting planar surfaces. Such resonance behaviors exist in metallic gratings with subwavelength apertures, where standing electromagnetic waves are set up inside the cavity by the surface plasmons on the upper and lower walls of the slit [22, 29]. Besides SPP, cavity resonances occurring inside the holes have been the other "device" suggested to be responsible for enhanced light transmission through hole arrays [30–32].

There have been many articles written on this subject, and a brief survey is offered. Using equivalent circuit theories and the impedance matching concept, [33] presented an approach to interpret ET through subwavelength hole arrays which was, at that time, alternative to other contemporary forms of explanations. How the various circuit elements are related to geometrical parameters and in what ways they account for physical phenomena were also motivated and explained. This work was then extended in [34] to the treatment of infinitely long slits, this time also incorporating means to account for metal losses. In [35], the lumped-element approach was extended to the treatment of different dielectric slabs placed on the input and output faces of the perforated screen, used thereafter as the vehicle for the study of ET in the context of surface-wave modes in grounded slabs. The work in [36] relayed the prospects of using stacked hole arrays to create left-handed metamaterials. A thorough and comprehensive work is found in [37], which possesses full-wave rigor, considers oblique incidences, offers field solutions, includes losses through finite metal conductivity, and investigates stacked screens. The main aspect of the short paper in [38] is the emphasis of the role played by the number of holes in affecting the amplitude of the transmission through perforated screens, as demonstrated both by theory and experiment in that work. In [39], a subwavelength hole array sandwiched between two dielectric slabs was investigated. This work was then extended to transient waves in [40]. In [41], finite subwavelength hole arrays were studied by a theoretical framework that manages even aperiodic distributions of arbitrarily-positioned holes, each with generally different properties (shape, size, material-filling). The work of [42] treated rectangular hole arrays and also discussed the limitation imposed by absorption losses into the metal on the transmission resonance. Using the 3D FDTD method, [43] studied optical transmission properties of subwavelength hole-arrays, with particular focus on the effects which the permittivity of the dielectric filling the holes have on the transmission. Sophisticated implementations of methods for treating periodic structures in the same context have been reported in [44–46]. Besides theoretical studies, experimental works on this topic of extraordinary transmission have also been performed in numerous papers such as those of [11, 32, 47–49]. Circuit models were also employed in [50] and [51] for treating related but unidentical structures, namely and respectively, an array of nanowires embedded within a dielectric host and a one-dimensional array of metallic strips. The study in the former had assumed the premise of normal incidence and one polarization only whereas the validity of the approach proposed in the latter is restricted to frequencies below the cutoff frequency of the first higher order mode inside the slits, limitations which are not suffered by the full-wave modal method that is presented herein. Nonetheless, being based on circuit models, the techniques in both those aforementioned papers are believed to be simpler to formulate and code up in computer programs and may also be potentially more computationally efficient.

Despite the postulated ascription of exceptional transmission through hole arrays in metallic screens to SPP effects, there still has not been concrete technical demonstration of just how or why this is actually the case. Particularly, present explanations of the phenomena are not yet unequivocally convincing, either lacking of theoretical proofs in mathematical forms or falling short of graphical portrayal. This paper attempts to strengthen the account for the mechanism by linking up two classical scientific diagrams: (1) the modal surface-wave dispersion graph, and (2) the Floquet lattice diagram (both for the hole array) with the peaks in the transmission spectra of the perforated screen, thereby offering a substantive way of associating extraordinary surges in wave penetration with surface-wave resonances. Moreover, most if not all present studies of the topic have only considered normal incidences of the illuminating wave. Here, oblique directions of arrival shall be investigated as well. In addition, the

polarization of the incident wave will also be taken into account, an aspect which is absent in previous efforts.

The aforementioned graphs of the transmission coefficient versus frequency (transmission spectra) and the surface-wave modal dispersion diagrams are herein generated from the numerical solutions obtained by a rigorous full-wave modal treatment of the rectangular hole array in a conducting sheet, which uses the moment method entailing Green's functions for rectangular cavities and planar multilayer structures in the spectral domain. The details of this approach are given in the upcoming section.

2. MODAL ANALYSIS — THEORY AND FORMULATION

Consider an incident plane wave that is impingent on a penetrable rectangular hole array pierced into an infinite PEC (perfect electric conducting) planar sheet of finite thickness d, as depicted by Fig. 1, in which a reference coordinate system is also shown. The width and height of each hole are respectively a and h along x and y, with the periods of the lattice being d_x and d_y. The direction of arrival relative to the structure is characterized by the angles denoted as θ_{inc} and ϕ_{inc} measured respectively from the z and x axes, the latter azimuth angle defining the plane of incidence as portrayed by the tilted sheet in the drawing.

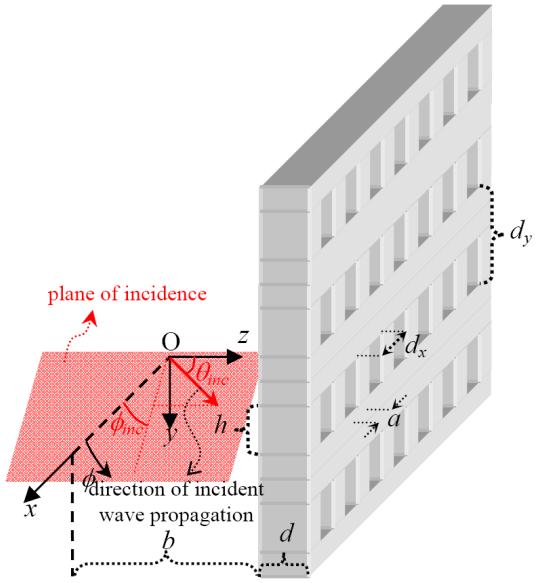

Figure 1. Schematic and geometry of rectangular hole array illuminated by incident plane wave, with plane of incidence defined by (θ_{inc}, ϕ_{inc}).

2.1. PEC-Equivalent Cavity-Aperture Magnetic Current

With reference to Fig. 1, the total component of the electric field parallel with the transverse xy plane as observed over any one of the two scattering cavity apertures at $z = b$ or $b + d$ is expressed as:

$$\vec{e}_t^{cav}(x_o, y_o) = \sum_{pqr=1}^{N_{cav}} A_{pqr} \vec{e}_{t_{pqr}}^{cav}(x_o, y_o); \quad \vec{e}_{t_{pqr}}^{cav} = \hat{x} e_{x_{pqr}}^{cav} + \hat{y} e_{y_{pqr}}^{cav} \tag{1}$$

in which e_t represents the transverse modal electric field vector function of the rectangular waveguide with the same $a \times h$ cross section along x and y as the cavity apertures, and pqr denotes the modal triple-index, p and q being integers as of $p\pi/a$ and $q\pi/h$, while r signifies TE or TM. The total number of waveguide modes considered for representing the fields over each cavity-aperture is labeled as N_{cav}. Evidently, A_{pqr} symbolizes the modal amplitude coefficients, being thus far unknown and to be solved

for. Consequently, the PEC-equivalent magnetic current densities over the cavity apertures are given by:

$$\left[\begin{array}{c} M_x^{z_s=\{{}_b^{b+d}\}} \\ M_y^{z_s=\{{}_b^{b+d}\}} \end{array}\right] = \sum_{pqr=1}^{N_{cav}} A_{pqr}^{z=\{{}_b^{b+d}\}} \left[\begin{array}{c} \pm e_{y_{pqr}}^{cav} \\ \mp e_{x_{pqr}}^{cav} \end{array}\right] \tag{2}$$

in which the upper and lower items within superscripted curly braces correspond respectively to the upper and lower signs of the $\pm$ symbol prefixing the e field functions on the right-hand side of the equation. These waveguide modal transverse electric field functions are in their orthonormalized forms, as required of the dyadic cavity Green's functions, and whose explicit expressions are furnished in Appendix A. The Fourier transforms of the magnetic currents in Eq. (2) into the spectral $(k_x,\ k_y)$ domain are written as

$$\left[\begin{array}{c} \tilde{M}_x^{z_s=\{{}_b^{b+d}\}}(k_x,k_y) \\ \tilde{M}_y^{z_s=\{{}_b^{b+d}\}}(k_x,k_y) \end{array}\right] = \sum_{pqr=1}^{N_{cav}} A_{pqr}^{z=\{{}_b^{b+d}\}} \left[\begin{array}{c} \pm\tilde{e}_{y_{pqr}}^{cav}(k_x,k_y) \\ \mp\tilde{e}_{x_{pqr}}^{cav}(k_x,k_y) \end{array}\right] \tag{3}$$

$$\tilde{e}_{w_{pqr}}^{cav}(k_x,k_y) = \int_{y=-\frac{h}{2}}^{y=\frac{h}{2}} \int_{x=-\frac{a}{2}}^{x=\frac{a}{2}} e_{w_{pqr}}^{cav}(x,y) e^{j(k_x x + k_y y)} dx dy \tag{4}$$

where w may be x or y.

2.2. Fields Radiated by PEC-Equivalent Cavity-Aperture Magnetic Currents into Various Regions

2.2.1. Left: $-\infty < z < b$ (Incidence Region)

For the left semi-infinite (incident) region within which the plane wave impingent on the hole array emerges, where a single homogeneous medium is concerned, the pertinent multilayer configuration for the core-routine of the numerical spectral-domain multilayer Green's function (details of which are precluded here but found in [52]) is simply a two-layer scenario with interface at $z = b$ comprising a PEC semi-infinite upper half-space layer that extends up to $z = +\infty$ and a lower likewise semi-infinite half-space layer made of the material constituting the left semi-infinite (incident) region that stretches down to $z = -\infty$. But in anticipation of possible subsequent analysis of multiple dielectric layers incorporated over the input side of the hole array for potential enhancement of transmission, a five-layer configuration shall instead be considered, as shown in Fig. 2(a), being just a showcased topology that is highly practical and more than adequate for almost all foreseeable scenarios of stratification, although the upcoming formulation is valid for any other number of layers. The central third layer is labeled as the ith layer, with the other layer indices with respect to this $i = 3$, e.g., the first lowermost layer without a lower bound is the $(i-2)$th layer while the topmost fifth one (PEC) that is unbounded above is tagged as the $(i+2)$th layer. The z-level of the upper boundary of the ith layer is indicated as z_i.

The scattered fields within this left-side incidence region are caused by the spectral current sources at the upper boundary $z = z_{i+1} = z_4 = +b$ of Fig. 2(a), being the Fourier-transformed PEC-equivalent cavity-aperture magnetic currents relayed in the preceding Subsection 2.1.

The following (pqr)th modal basis functions for expanding the magnetic currents over the cavity aperture at $z = b + d$ with $+\hat{z}$ as the outward unit normal and their Fourier-transformed spectral forms are first defined:

$$m_{\{{}_y^x\}_{pqr}}(x,y) = \pm e_{\{{}_x^y\}_{pqr}}^{cav}(x,y); \quad \tilde{\tilde{m}}_{\{{}_y^x\}_{pqr,mn}}^{=} \pm \tilde{\tilde{e}}_{\{{}_x^y\}_{pqr}}^{cav}(k_{x_m}, k_{y_m}) \tag{5}$$

in which the upper and lower signs of $\pm$ correspond to the upper and lower symbols within the subscripted curly braces. By virtue of the discrete spectrum of the presently considered periodicity with periods along x and y being d_x and d_y, these above Fourier-transformed modal basis current functions are evaluated at discrete values of k_x and k_y governed by

$$k_{x_m} = k_{x_{m=0}} + 2m\pi/d_x \quad \text{and} \quad k_{y_n} = k_{y_{n=0}} + 2n\pi/d_y, \tag{6}$$

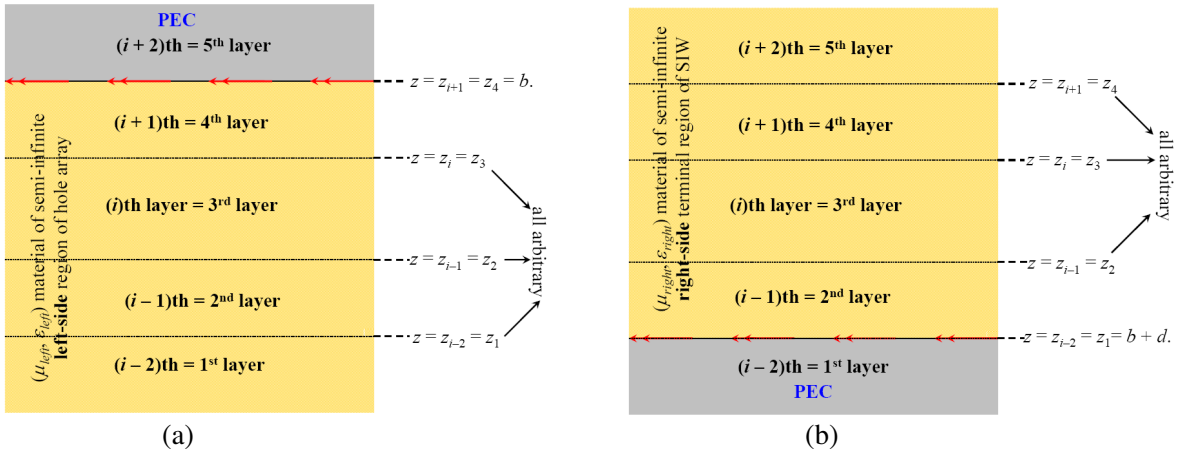

Figure 2. Five-layer configuration for (a) left semi-infinite (incident) region, and (b) right semi-infinite (transmission) region of rectangular hole-array used in core-routine of spectral multilayer Green's function.

with m and n being integers, and

$$k_{x_{m=0}} = k_i \sin\theta_0 \cos\phi_0 \quad \text{and} \quad k_{y_{n=0}} = k_i \sin\theta_0 \sin\phi_0 \tag{7}$$

where $k_i = 2\pi f\sqrt{\mu_i \varepsilon_i}$. The angles θ_0 and ϕ_0 are measured from the z and x axes respectively and they define the direction of the (0, 0)th dominant Floquet modal plane wave, being the incident plane wave in the present context, whose wavenumbers along x and y are $k_{x_{m=0}}$ and $k_{y_{n=0}}$, constituting the forcing wavenumbers along x and y respectively.

The spatial-domain fields in the ℓth layer ($\ell = 1$, 2, 3 or 4) of Fig. 2(a) are represented by

$$F^{(\ell)left}_{w_{M^{z=b}_{x+y}}}(x,y,z) = F'^{(\ell)left}_{w_{M^{z=b}_{x+y}}}(z) e^{-j(k_{x_m}x + k_{y_n}y)} \tag{8a}$$

$$F'^{(\ell)left}_{w_{M^{z=b}_{x+y}}}(z) = \frac{1}{d_x d_y} \sum_{pqr=1}^{N_{cav}} A^{z=b}_{pqr} \sum_{mn=1}^{MN} \tilde{\tilde{G}}^{(\ell)left}_{F_w} \cdot \left(\tilde{\tilde{m}}^{z^{ex}_{i+1}=b}_{x_{pqr,mn}} + \tilde{\tilde{m}}^{z^{ex}_{i+1}=b}_{y_{pqr,mn}} \right) \tag{8b}$$

$$\tilde{\tilde{m}}^{z^{ex}_{i+1}=b}_{\{x\}_{pqr,mn}} = \tilde{\tilde{m}}_{\{x\}_{pqr,mn}} \tag{9}$$

noting that the exponential term of Eq. (8a) with m and n indices is within the summation over the Floquet modal harmonic index mn in Eq. (8b). The field symbol F is E or H, and w is x, y or z. The symbol $\tilde{\tilde{G}}$ represents the spectral multilayer Green's function that operates on the spectral modal basis current functions of Eq. (5) which now have superscripted indications of their z-locations (Fig. 2(a)), thereby giving the associated spectral field component F_w (as subscripted in $\tilde{\tilde{G}}$) radiated by them. Notice that a '*left*' superscript has been added to signify that the five-layer configuration of Fig. 2(a) for the left semi-infinite incidence region is used in the core routine, with the topmost layer made of PEC. Also note the distinction between indices ℓ and i, respectively for the index of the layer (in Fig. 2(a)) in which the field F is observed and that of the one within which the (mn)th spectral (pqr)th basis magnetic current source $\tilde{\tilde{m}}_{w_{pqr,mn}}$ is located.

2.2.2. Right: $b + d < z < \infty$ (Transmission Region)

As for the left-side (incidence) region, the pertinent multilayer configuration of the spectral multilayer core routine for a homogeneous right-side (transmission) region is also simply a two-layer scenario, this time with interface at $z = b + d$ comprising a lower semi-infinite half-space PEC layer that reaches down to $z = -\infty$ (i.e., spans from $z = -\infty$ to $z = b + d$) and an upper likewise semi-infinite half-space layer made of the material constituting the right semi-infinite (transmission) side region of the SIW

that extends up to $z = +\infty$ (i.e., exists from $z = b + d$ to $z = +\infty$). But retaining the same liberty of stratifying the right-side region with four different media as well, the five-layer configuration of Fig. 2(b) is applied to the core-routine of the spectral multilayer Green's function.

The PEC-equivalent magnetic cavity-aperture currents responsible for driving the core routine are now located on the lower boundary at $z = z_{i-2} = z_1 = b + d$, just within the $(i-1)$th = 2nd layer. In a similar fashion as Eqs. (8a), (8b), and (9), the fields in the ℓth layer ($\ell = 2$, 3, 4 or 5) of Fig. 2(b), are given by

$$F^{(\ell)right}_{w_{M^{z=b+d}_{x+y}}}(x,y,z) = F'^{(\ell)right}_{w_{M^{z=b+d}_{x+y}}}(z) e^{-j(k_{x_m}x + k_{y_n}y)} \tag{10a}$$

$$F'^{(\ell)right}_{w_{M^{z=b+d}_{x+y}}}(z) = \frac{1}{d_x d_y} \sum_{pqr=1}^{N_{cav}} A^{z=b+d}_{pqr} \sum_{mn=1}^{MN} \tilde{\tilde{G}}^{(\ell)right}_{F_w} \cdot \left(\tilde{\tilde{m}}^{z^{ex}_{i-1}=b+d}_{x_{pqr,mn}} + \tilde{\tilde{m}}^{z^{ex}_{i-1}=b+d}_{y_{pqr,mn}} \right) \tag{10b}$$

$$\tilde{\tilde{m}}^{z^{ex}_{i-1}=b+d}_{\{x\}_{pqr,mn}} = \tilde{\tilde{m}}_{\{x\}_{pqr,mn}} \tag{11}$$

2.3. Boundary Conditions: Continuity of Tangential Magnetic Field Component across Cavity Apertures

Through the sign cases of Eq. (2), depending on whether the PEC-equivalent cavity-aperture magnetic current is right or left facing, i.e., with the unit normal pointing towards the region into which fields are radiated being $+\hat{z}$ or $-\hat{z}$, the continuities of the tangential electric field components across the various cavity apertures are already implicitly satisfied. What remains is then to enforce the continuity of the tangential magnetic field component.

2.3.1. Input (Left) Aperture at $z = b$

The boundary condition for this case is given by:

$$\begin{aligned} &\hat{x}\left[H^{(\ell=4)left}_{x_{M^{z=b}_{x+y}}} + \tilde{\tilde{G}}^{(\ell=4)left}_{H_x} \cdot \Psi^{z^{ex1^\circ}_{\tau=i}}_{\sigma} e^{-j\left(k_{x_0}x + k_{y_0}y\right)} \right]_{z=b} + \hat{y}\left[H^{(\ell=4)left}_{y_{M^{z=b}_{x+y}}} + \tilde{\tilde{G}}^{(\ell=4)left}_{H_y} \cdot \Psi^{z^{ex1^\circ}_{\tau=i}}_{\sigma} e^{-j\left(k_{x_0}x + k_{y_0}y\right)} \right]_{z=b} \\ &= \sum_{pqr=1}^{N_{cav}} \left[A^{z=b}_{pqr} \coth\left(\gamma^{cav}_{z_{pqr}} d\right) - A^{z=b+d}_{pqr} \operatorname{csc} h\left(\gamma^{cav}_{z_{pqr}} d\right) \right] \vec{h}^{cav}_{t_{pqr}}(x,y;z=b) \end{aligned} \tag{12}$$

with the $(x,\ y)$ observation coordinates [albeit not explicit in the first two terms within parentheses on the left-hand side of this equation] being over the left-side input cavity aperture at $z = b$ with $-a/2 < x < a/2$, $-h/2 < y < h/2$. The symbol $\Psi^{z^{ex1^\circ}_{\tau=i}}_{\sigma}$ (Ψ is J or M and σ may be x, y or z) represents the primary (1°) excitation source that is assumed to be located at $z = z^{ex1^\circ}_{\tau=i}$ within the τth = ith = 3rd layer (middle part) of Fig. 2(a) for the left-side incidence region. The subscript $z = b$ attached to the square brackets signify that the H-fields are observed at those z-levels. The right-hand side of Eq. (12) is acquired by the dyadic cavity Green's functions.

2.3.2. Output (Right) Aperture at $z = b + d$

The boundary condition for this interface is written as:

$$\begin{aligned} &\hat{x}\left[H^{(\ell=2)right}_{x_{M^{z=b+d}_{x+y}}} \right]_{z=b+d} + \hat{y}\left[H^{(\ell=2)right}_{y_{M^{z=b+d}_{x+y}}} \right]_{z=b+d} \\ &= \sum_{pqr=1}^{N_{cav}} \left[A^{z=+b}_{pqr} \operatorname{csc} h\left(\gamma^{cav}_{z_{pqr}} d\right) - A^{z=b+d}_{pqr} \coth\left(\gamma^{cav}_{z_{pqr}} d\right) \right] \vec{h}^{cav}_{t_{pqr}}(x,y;z=b+d) \end{aligned} \tag{13}$$

with the $(x,\ y)$ observation coordinates being over the right-end output aperture of the cavity at $z = b+d$, and noticing this time the absence of the primary excitation source term on the left-hand side unlike Eq. (12) for the input side. As before, the functional dependencies (arguments) on the $(x,\ y)$ observation coordinates of the H_w fields on the left-hand side are not explicitly shown.

2.4. Galerkin Weighting: Generate System of Equations

Taking $\int_{y=-h/2}^{y=h/2}\int_{x=-a/2}^{x=a/2} \vec{e}_{t_{rst}}^{cav}(x,y) \times \_\_\_ \cdot \hat{z}dxdy$ throughout Eqs. (12), and (13), each for $rst = 1, 2, \ldots, N_{cav}$, the following two equations are respectively obtained.

$$\left[H'^{(\ell=4)left}_{y_{M^{z=b}_{x+y}}}\right]_{z=b} \tilde{\tilde{e}}^{cav}_{x_{rst}}(-k_{x_m},-k_{y_n}) + \left[\tilde{\tilde{G}}^{(\ell=4)left}_{H_y} \cdot \Psi^{z^{ex1^\circ}_{\tau=i}}_{\sigma}\right]_{z=b} \tilde{\tilde{e}}^{cav}_{x_{rst}}(-k_{x_0},-k_{y_0})$$
$$- \left[H'^{(\ell=4)left}_{x_{M^{z=b}_{x+y}}}\right]_{z=b} \tilde{\tilde{e}}^{cav}_{y_{rst}}(-k_{x_m},-k_{y_n}) - \left[\tilde{\tilde{G}}^{(\ell=4)left}_{H_x} \cdot \Psi^{z^{ex1^\circ}_{\tau=i}}_{\sigma}\right]_{z=b} \tilde{\tilde{e}}^{cav}_{y_{rst}}(-k_{x_0},-k_{y_0})$$
$$= A^{z=b}_{rst}\coth\left(\gamma^{cav}_{z_{rst}}d\right) - A^{z=b+d}_{rst}\csc h\left(\gamma^{cav}_{z_{rst}}d\right) \tag{14}$$

$$\left[H'^{(\ell=2)right}_{y_{M^{z=b+d}_{x+y}}}\right]_{z=b+d} \tilde{\tilde{e}}^{cav}_{x_{rst}}(-k_{x_m},-k_{y_n}) - \left[H'^{(\ell=2)right}_{x_{M^{z=b+d}_{x+y}}}\right]_{z=b+d} \tilde{\tilde{e}}^{cav}_{y_{rst}}(-k_{x_m},-k_{y_n})$$
$$= A^{z=+b}_{rst}\csc h\left(\gamma^{cav}_{z_{rst}}d\right) - A^{z=b+d}_{rst}\coth\left(\gamma^{cav}_{z_{rst}}d\right) \tag{15}$$

whereby all right-hand sides are the result of waveguide mode orthonormality, as established in Appendix A. These generate a total of $2N_{cav}$ equations sufficient for solving this same total number of unknown modal amplitude coefficients.

2.5. Construction of Matrix Equation

Anticipating the sequence of the unknown amplitude modal coefficients as placed in the $4N_{cav} \times 1$ column-vector:

$$\bar{V} = \left\{ \begin{array}{c} \left[\begin{array}{ccc} z=+b & & z=+b \\ A^{cav}_{pqr=1} & \cdots & A^{cav}_{pqr=N_{cav}} \end{array} \right]^T \\ \left[\begin{array}{ccc} z=b+d & & z=b+d \\ A^{cav}_{pqr=1} & \cdots & A^{cav}_{pqr=N_{cav}} \end{array} \right]^T \end{array} \right\}_{2N_{cav}\times 1} \tag{16}$$

with the non-conjugate transpose operators "T" merely for compactness and thus saving manuscript space (prevent taking up excessive space vertically downwards), the upcoming matrix operations are performed. Defining $\kappa = 1/(d_x d_y)$, using underscores to signify that their associated quantities are matrices, parenthesized row and column index symbols explicitly indicating the structural forms of the matrices, and with w being x or y, the following matrices are constructed.

$$\left[\underset{\sim}{\tilde{H}}'^{(\ell=4)left}_{w_{M^{z=b}_{x+y}}}(mn,pqr)\right]_{MN\times N_{cav}} = \kappa\left[\tilde{\tilde{G}}^{(\ell=4)left}_{H_w} \cdot \left(\tilde{\tilde{m}}^{z^{ex}_{i+1}=b}_{x_{pqr,mn}} + \tilde{\tilde{m}}^{z^{ex}_{i+1}=b}_{y_{pqr,mn}}\right)\right]_{z=b}$$

$$\left[\underset{\sim}{\tilde{H}}'^{(\ell=2)right}_{w_{M^{z=b+d}_{x+y}}}(mn,pqr)\right]_{MN\times N_{cav}} = \kappa\left[\tilde{\tilde{G}}^{(\ell=2)right}_{H_w} \cdot \left(\tilde{\underset{\sim}{m}}^{z^{ex}_{i-1}=b+d}_{x_{pqr,mn}} + \tilde{\underset{\sim}{m}}^{z^{ex}_{i-1}=b+d}_{y_{pqr,mn}}\right)\right]_{z=b+d}$$

$$\left[\tilde{\tilde{e}}^{*}_{w_{rst}}(rst,mn)\right]_{N_{cav}\times MN} = \tilde{\tilde{e}}^{cav}_{w_{pqr}}(-k_{x_m},-k_{y_n})$$

$$[\{\Upsilon\}(rst,rst)] = \left[\begin{array}{cccc} \left\{\begin{array}{c}\coth\\ \csc h\end{array}\right\}\left(\gamma^{cav}_{z_{rst=1}}d\right) & 0 & \cdots & 0 \\ 0 & \left\{\begin{array}{c}\coth\\ \csc h\end{array}\right\}\left(\gamma^{cav}_{z_{rst=2}}d\right) & \cdots & 0 \\ \vdots & \vdots & \ddots & \vdots \\ 0 & 0 & \cdots & \left\{\begin{array}{c}\coth\\ \csc h\end{array}\right\}\left(\gamma^{cav}_{z_{rst=N_{cav}}}d\right) \end{array}\right]$$

such that:

$$[M_{11}]_{N_{cav}\times N_{cav}} = \left[\tilde{\tilde{e}}^{*}_{x_{pqr}}(rst,mn)\right]_{N_{cav}\times MN}\left[\underset{\sim}{\tilde{H}}'^{(\ell=4)left}_{y_{M^{z=b}_{x+y}}}(mn,pqr)\right]_{MN\times N_{cav}}$$
$$- \left[\tilde{\tilde{e}}^{*}_{y_{pqr}}(rst,mn)\right]_{N_{cav}\times MN}\left[\underset{\sim}{\tilde{H}}'^{(\ell=4)left}_{x_{M^{z=b}_{x+y}}}(mn,pqr)\right]_{MN\times N_{cav}} - [\Upsilon(rst,rst)]_{N_{cav}\times N_{cav}}$$

$$[M_{12}]_{N_{cav}\times N_{cav}} = [(rst,rst)]_{N_{cav}\times N_{cav}} = -[M_{21}]_{N_{cav}\times N_{cav}}$$

$$[M_{22}]_{N_{cav}\times N_{cav}} = \left[\tilde{\tilde{e}}^{*}_{x_{pqr}}(rst,mn)\right]_{N_{cav}\times MN}\left[\tilde{H'}^{(\ell=2)right}_{y_{M^{z=b+d}_{x+y}}}(mn,pqr)\right]_{MN\times N_{cav}}$$
$$-\left[\tilde{\tilde{e}}^{*}_{y_{pqr}}(rst,mn)\right]_{N_{cav}\times MN}\left[\tilde{H'}^{(\ell=2)right}_{x_{M^{z=b+d}_{x+y}}}(mn,pqr)\right]_{MN\times N_{cav}} + [\Upsilon(rst,rst)]_{N_{cav}\times N_{cav}}$$

$$\left[\mathrm{X}^{(4)}(rst,1)\right]_{N_{cav}\times 1} = \left[\tilde{\tilde{G}}^{(\ell=4)left}_{H_y}\cdot\Psi^{z^{ex1^{\circ}}_{\tau=i}}_{\sigma}\right]_{z=b}\tilde{\tilde{e}}^{cav}_{x_{rst}}(-k_{x_0},-k_{y_0}) - \left[\tilde{\tilde{G}}^{(\ell=4)left}_{H_x}\cdot\Psi^{z^{ex1^{\circ}}_{\tau=i}}_{\sigma}\right]_{z=b}\tilde{\tilde{e}}^{cav}_{y_{rst}}(-k_{x_0},-k_{y_0})$$

Subsequently, the ultimate matrix equation is generated as:

$$\bar{M}\bar{V} = \bar{X} \tag{17}$$

$$\bar{M} = \left\{ \begin{array}{cc} [M_{11}]_{N_{cav}\times N_{cav}} & [M_{12}]_{N_{cav}\times N_{cav}} \\ [M_{21}]_{N_{cav}\times N_{cav}} & [M_{22}]_{N_{cav}\times N_{cav}} \end{array} \right\}_{2N_{cav}\times 2N_{cav}} \tag{18}$$

$$\bar{X} = -\left\{ \left(\begin{array}{cc} \left[\mathrm{X}^{(4)}(rst,1)\right]^{T} & [\mathrm{zeros}]_{1\times N_{cav}} \end{array} \right)^{T} \right\}_{2N_{cav}\times 1} \tag{19}$$

where again the non-conjugate transpositions involved in the latter vector are just to avoid using up too much space vertically downward. This final matrix equation may then be solved for the modal amplitude coefficients in $\bar{V}$ simply by matrix inversion, tools for which are already built in within most if not all modern computer programming software.

3. SCREEN POROSITY AND TRANSMISSION EFFICIENCY

To facilitate the upcoming developments, amongst the foremost quantities to establish is the screen *porosity*, $\wp$, defined as the ratio of the area of the rectangular hole to that of the unit cell, which in the present context is

$$\wp = ah/d_x d_y, \tag{20}$$

In the most physically intuitive sense, the usual zeroth-order transmission coefficient, T, defined as the fraction of the incident power that is transmitted through the perforated screen by the dominant ($m = 0$, $n = 0$)th Floquet harmonic mode, is then equal to the porosity $\wp$, since it is indeed just this proportion of the screen that receives (or 'feels') the impingent radiation and is thus permeable. If T is less than $\wp$, then it is still a conceivable outcome since there is certainly the logical possibility of imperfections (such as reflective or dissipative losses) such that some of the incident power fails to get through the screen. However, if T exceeds $\wp$, more output power than the available input amount collected by the holes penetrates the screen, resulting in an unusual phenomenon; an *extraordinary transmission*. Therefore, a so-called *transmission efficiency*, ε_T, may be defined as the ratio of T to $\wp$, i.e.,

$$\varepsilon_T = T/\wp, \tag{21}$$

In this way, when T equals $\wp$, the latter serving as an apparent upper limit, a 100% efficiency arises, amounting to nothing more than what is expected of a lossless perfect screen; what goes into the holes gets out of them on the other side. If T falls short of $\wp$, the notion of losses sets in, falling in line with an ε_T that is understandably less than unity. But if T is larger than $\wp$, an extraordinary efficiency greater than 100% results.

4. DEMONSTRATION OF EXTRAORDINARY TRANSMISSION

With the formulation of Section 2, the plane-wave scattering by the rectangular hole-array can be analyzed, from which the reflection and transmission coefficients may be acquired.

4.1. Normal Incidence

With reference to the geometry of Fig. 1, the parameters of the rectangular hole-array in the ambience of free space that have been computed for the demonstration of extraordinary transmission are as follows: square unit cell with period $d_x = d_y = d_{x\&y} = 5\,\text{mm}$, likewise square hole with dimensions $a = h = 2.5\,\text{mm}$, and the thickness of the perforated PEC screen is $d = 1.25\,\text{mm}$. The consequent screen *porosity*, $\wp$, as defined in (20), has a value of 0.25. Intuitively, for illumination by normally incident plane waves, this porosity represents the upper limit of the transmission coefficient, since it is effectively only this fraction of the incoming radiation that impinges on the holes. The so-called *transmission efficiency* is thereby defined, according to Eq. (21), as the ratio of the transmission coefficient to the screen porosity, presumably with a maximum of unity (100%).

Referring again to Fig. 1 for the angular coordinates, for a TM^z polarized plane wave impingent on the hole array with angles of incidence $\theta_{inc} = 0$ (normal incidence) and $\phi_{inc} = 90^\circ$ (yz plane of incidence), consequently entailing the E_y and H_x transverse field components, the graph of the power transmission coefficient versus frequency for the dominant zeroth Floquet modal order acquired from the modal analysis of the preceding Section 2 is presented in Fig. 3(a), alongside the corresponding plot generated by CST simulations. Evidently, good agreement between the modal approach and the commercial software is achieved.

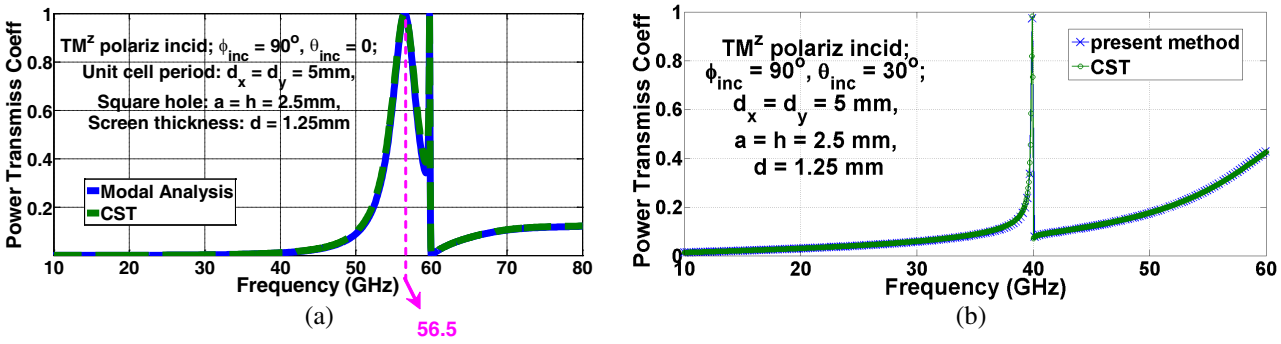

Figure 3. Validation with CST of modal formulation for zeroth-order power transmission coefficient versus frequency of TMz polarized plane wave incident on square hole array with unit cell period (lattice constant): $d_x = d_y = d_{x\&y} = 5\,\text{mm}$, square hole size: $a = h = 2.5\,\text{mm}$, and screen thickness $d = 1.25\,\text{mm}$, for (a) $\phi_{inc} = 90^\circ$, $\theta_{inc} = 0$ and (b) $\phi_{inc} = 90^\circ$, $\theta_{inc} = 30^\circ$.

Two distinct peaks in the transmission plot of Fig. 3(a) are observed, one at $f^-_{d_{x\&y}=\lambda}$ just incrementally below $f_{d_{x\&y}=\lambda} = 60\,\text{GHz}$ at which the wavelength equals the lattice constant (square cell period $d_{x\&y} = 5\,\text{mm}$), and another at around 56.5 GHz, henceforth denoted as f^*. And just minutely above $f_{d_{x\&y}=\lambda}$, at $f^+_{d_{x\&y}=\lambda}$, the transmission undergoes a sharp dip. Explanations of both peaks and the dip shall be given in the upcoming subsections. Before that, a further validation case is given in Fig. 3(b) for the same screen and polarization with $\phi_{inc} = 90^\circ$ but now for oblique incidence of $\theta_{inc} = 30^\circ$.

4.1.1. Sharp Dip in Transmission at Frequency Just Slightly above the One at Which Cell-Size Equals Wavelength

Consider first, Fig. 4 in which the lattice arrangement of Floquet harmonic modal nodes is masked onto the spectral k_x-k_y plane. Synonymous to the so-called grating lobe diagram in antenna array theory, the spacings between adjacent nodes along the k_x and k_y dimensions are $2\pi/d_x$ and $2\pi/d_y$ respectively (for the presently considered square cell, a periodic nodal array of likewise square cells is depicted). The location of the (m, n)th diffraction order is defined by:

$$k_{xm} = k_{x0} + 2m\pi/d_x \quad \text{and} \quad k_{yn} = k_{y0} + 2n\pi/d_y, \tag{22}$$

$$k_{x0} = k_0 \sin\theta_{inc} \cos\phi_{inc} \quad \text{and} \quad k_{y0} = k_0 \sin\theta_{inc} \sin\phi_{inc} \tag{23}$$

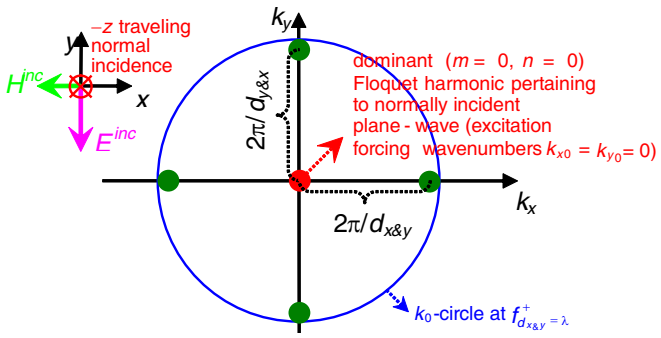

Figure 4. Lattice arrangement of Floquet harmonic modal nodes on grating lobe diagram (in k_x-k_y spectral plane) for unit cell periods $d_x = d_y = d_{x\&y} = 5\,\text{mm}$, with internodal spacing being $2\pi/d_x$ and $2\pi/d_y$ along k_x and k_y. Dominant ($m = n = 0$) zeroth order node at the origin (excitation forcing wavenumbers $k_{x0} = k_{y0} = 0$), indicated as a red dot, pertains to normally incident plane-wave in scattering scenario, and defines nodal locations of all other (m, n)th higher-order modes: $k_{xm} = k_{x0} + 2m\pi/d_x$ and $k_{yn} = k_{y0} + 2n\pi/d_y$, with k_{x0} and k_{y0} being related to the incidence angles of the excitation (forcing) wave: $k_{x0} = k_0 \sin\theta_{inc} \cos\phi_{inc}$ and $k_{y0} = k_0 \sin\theta_{inc} \sin\phi_{inc}$. Circle of radius being free-space wavenumber at $f^+_{d_{x\&y}=\pi}$ as drawn.

the latter two being the so-called forcing wavenumber components of the dominant Floquet harmonic pertaining to the excitation, which are in terms of the incidence angles (θ_{inc}, ϕ_{inc}) of the forcing wave. By virtue of the presently considered normally incident plane-wave ($\theta_{inc} = 0$ and thus $k_{x0} = k_{y0} = 0$), the dominant ($m = n = 0$) zeroth order node is situated at the origin, indicated by the red dot in Fig. 4, with its four closest neighboring nodes shown as green nodes. Note that the transverse components of the $-z$ traveling TM^z polarized normally incident plane wave are also depicted in Fig. 4.

The radius of the origin-centered circle in Fig. 4 is the free-space wavenumber $2\pi f^+_{d_{x\&y}=\lambda}\sqrt{\mu_0\varepsilon_0}$ at $f^+_{d_{x\&y}=\lambda}$ where the sharp dip in transmission occurs, μ_0 and ε_0 being the free-space permeability and permittivity, respectively. Nodes that fall within this circle are associated with (fast) space waves radiating in real visible space, whereas those outside of it pertain to (slow) surface waves in so-called imaginary invisible space. At $f^+_{d_{x\&y}=\lambda}$, the four higher-order diffraction orders (green nodes in Fig. 4) are marginally in real visible space, thus representative of space-waves that graze the surface of the hole array. These tangentially propagating harmonics undergo a surge in their amplitudes, thereby 'sucking' energy away from the dominant Floquet mode (so-called "main beam" in array theory) that remains in visible real space, resulting in a severe drop in transmission level at $f^+_{d_{x\&y}=\lambda}$ at which the cell-size $d_{x\&y}$ is just slightly *larger* than the wavelength:$\lambda_{f^+_{d_{x\&y}=\lambda}} = c \Big/ f^+_{d_{x\&y}=\lambda}$, c being the velocity of light in vacuum. This is known as Rayleigh's minima of Wood's anomaly [53, 54], which states that when the hole-spacing approaches the wavelength, there could be no transmission.

4.1.2. Spike in Transmission at Frequency Just Slightly below the One at Which Cell-Period Equals Wavelength

Refer now to the Floquet diagram of Fig. 5, still with the same lattice configuration of the nodal array as Fig. 4 and the dominant modal node remaining at the origin. But this time, the radius of the k_0 circle is slightly smaller, being $2\pi f^-_{d_{x\&y}=\lambda}\sqrt{\mu_0\varepsilon_0}$, such that the diffraction harmonics, now being slow surface waves, are located just marginally in invisible space. Such disappearances of grazing space waves (as of Fig. 3(a)) from the visible regime lead to a redistribution of energy among the remaining Floquet modes in real space, which for the present case, is just the solitary dominant harmonic, thereby leading to a surge in the transmission level. There is actually another way to account for this rise, and that is through the surface-wave dispersion diagram. This is however deferred till the next subsection to which this form of explanation is more pertinent.

4.1.3. Extraordinary Transmission at Frequency Notably below the One at Which Period Equals Wavelength

Turning attention now to the grating lobe diagram of Fig. 6, this time with a k_0 circle of an even smaller radius $k_0^* = 2\pi f^* \sqrt{\mu_0 \varepsilon_0}$, where f^* is 56.5 GHz at which a transmission peak occurs (Fig. 3(a)). Now, all but the dominant Floquet harmonic node are exterior to the k_0 circle, thus representative of surface wave modes.

Using the same modal formulation of Section 2, the surface-wave dispersion diagram for the rectangular cavity hole array can be generated by numerical search for modal resonances among repeated solutions of numerous forcing wavenumbers. For TM^z polarized surface waves propagating along the y-direction defined by the azimuth angle $\phi_{00} = 90°$ measured from the x axis, the dispersion graph is given by Fig. 7(a), in which the straight line represents the light-line. Also shown as an inset drawing are the surface-wave propagation direction and the orientations of the associated field components, E_{00}^{ex} and H_{00}^{ex}, which are z and x directed, respectively, the latter sharing the same orientation as that of the presently-considered normally-incident TM^z polarized magnetic field, H^{inc}, impingent on the hole array

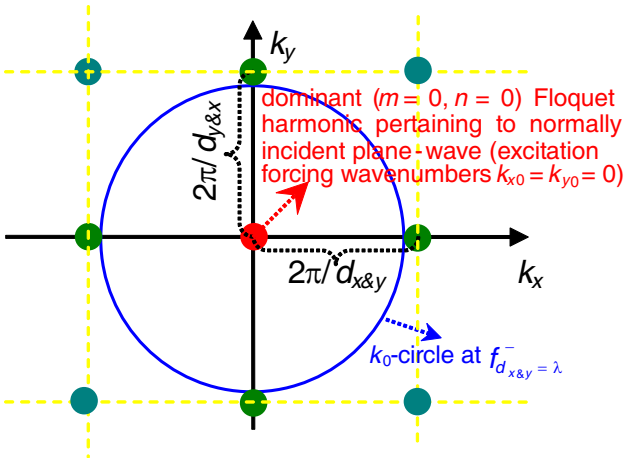

Figure 5. Grating lobe diagram for square cell ($d_{x\&y} = 5\,\text{mm}$) and with dominant Floquet node at origin (normal incidence). Circle radius equals free-space wavenumber at $f^-_{d_{x\&y}} = \lambda$.

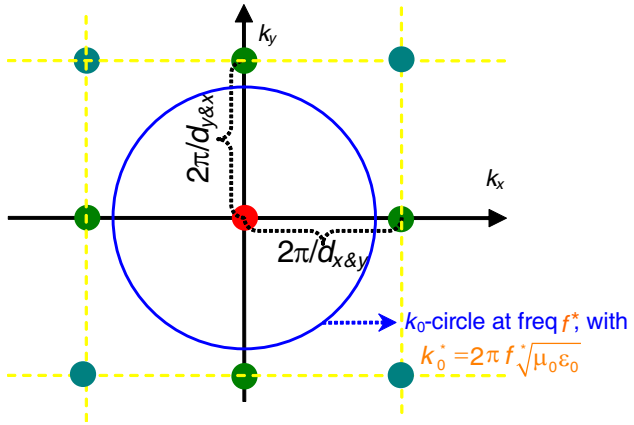

Figure 6. Grating lobe diagram for square cell ($d_{x\&y} = 5\,\text{mm}$) and with dominant Floquet node at origin (normal incidence). Circle radius equals free-space wavenumber at $f^* = 56.5\,\text{GHz}$. Schematic not drawn to scale.

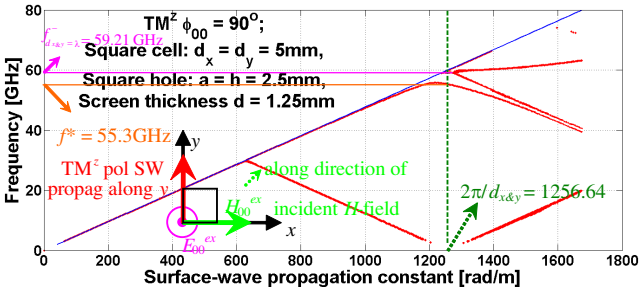

(a)

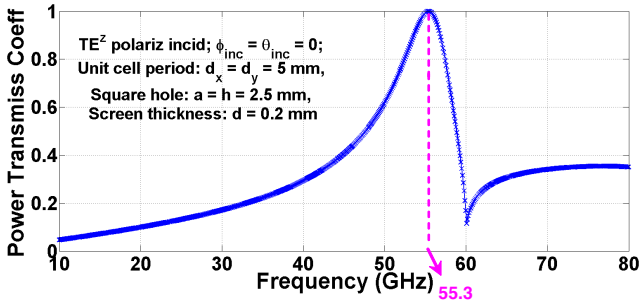

(b)

Figure 7. (a) Dispersion diagram of TMz polarized surface waves along $\phi_{00} = 90°$. Square cell: $d_x = d_y = 5\,\text{mm}$, square hole: $a = h = 2.5\,\text{mm}$, screen thickness $d = 1.25\,\text{mm}$, and (b) zeroth-order power transmission coefficient versus frequency of TM^z polarized plane wave incident on square hole array for $\phi_{inc} = 90°$, $\theta_{inc} = 0$ with unit cell period (lattice constant): $d_x = d_y = d_{x\&y} = 5\,\text{mm}$, square hole size: $a = h = 2.5\,\text{mm}$, and screen thickness $d = 0.2\,\text{mm}$ — much thinner than that of Fig. 3(a).

in the plane-wave scattering scenario. Consider next, the green dashed vertical line in Fig. 7(a) drawn through the abscissa value of $2\pi/d_{x\&y} = 1256.64$, which in the present context, corresponds particularly to the surface wavenumber of the $(m = 0, n = 1)$ Floquet harmonic surface wave propagating along the y direction (three other nodes share this same wavenumber). Modal dispersion traces intersect this line at two points with corresponding frequencies of 59.21 GHz and 55.3 GHz. Evidently, f^* (56.5 GHz) closely approximates the latter frequency at which a resonant surface wavenumber (being $2\pi/d_{x\&y} = 1256.64$) equals that of the $(m = 0, n = 1)$ harmonic. This surface-wave mode is thus resonant at f^* with strong magnitude, which flows along the y-direction on both sides of the perforated screen, thereby enhancing the transmission. Therefore, the incident plane wave of the scattering scenario is polarized in such a way that excites resonant surface waves along the y-direction ($\phi_{00} = 90°$ of the dispersion diagram in Fig. 7(a)) at f^*. The slight discrepancy between these latter two frequencies is due to the finite $d = 1.25$ mm screen thickness assumed in Fig. 3(a). When this thickness is reduced considerably to become $d = 0.2$ mm, the transmission spectrum becomes that of Fig. 7(b), which now indeed displays a peak at 55.3 GHz, thus coinciding perfectly with its associated dispersion diagram of Fig. 7(a), which exhibits a resonant surface wavenumber of 1256.64 rad/m at that very 55.3 GHz.

It is not difficult to tell, therefore, that the other frequency (59.21 GHz) pertains to $f^-_{d_{x\&y}=\lambda}$, the intersection point with which it is associated being indeed just within the slow-wave regime (very close to the light-line) of Fig. 7(a), as in Fig. 5. Hence at this frequency, all four harmonics at nodal locations: (0, 1), (1, 0), (−1, 0) and (0, −1) lying just beyond the periphery of the k_0 circle in Fig. 5, possess a common surface wavenumber ($2\pi/d_{x\&y} = 1256.64$) that exactly matches with a resonant wavenumber at that very same frequency, $f^-_{d_{x\&y}=\lambda}$ in the dispersion graph of Fig. 7(a). As a result, these strong surface-wave resonances give rise to strong transmission through the hole array.

4.1.4. Transmission Efficiency for Frequency Notably below the One at Which Period Equals Wavelength

The transmission efficiency, $\varepsilon_T^{actual} = T^{actual}/\wp$ according to Eq. (21), with T^{actual} being the actual power transmission coefficient, is plotted in Fig. 8. As $\wp = 0.25$, this graph of Fig. 8 over the range from 10 GHz to 80 GHz is thus simply that of Fig. 3(a) scaled by four times. As observed, with the exception of 120 GHz for which discussions shall be deferred, ε_T^{actual} remains less than 100% for frequencies above 60 GHz at which the wavelength equals the unit cell period, being a normal and expected phenomenon since the finite input power is distributed among more than just the dominant zeroth Floquet mode, i.e., powers are also channeled into higher-order Floquet harmonic plane waves that propagate in real visible space, thus leaving less power than the injected amount for the dominant zeroth-order Floquet mode (remember that T^{actual} is the transmission coefficient of the zeroth-order Floquet harmonic only). However, at the frequency just incrementally below 60 GHz, the transmission efficiency spikes up sharply (the reason of which as explained earlier) to acquire a value that is about 400% ($\approx 1/\wp$). As the frequency

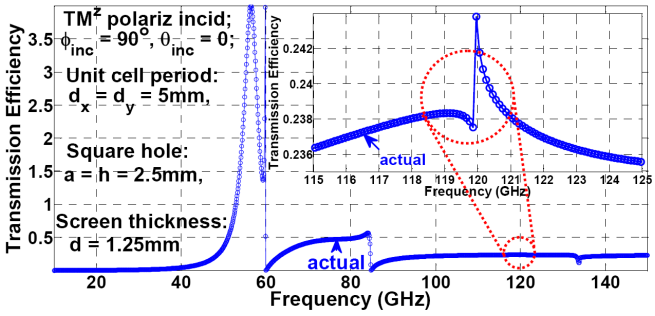

Figure 8. Transmission efficiencies, ε_T^{actual} & $\varepsilon_{T_{sq\,hole}}^{Bethe}$ versus frequency for a normally-incident TMz polarized plane wave (with $\phi_{inc} = 90°$) illuminating a square hole array with unit cell period (lattice constant): $d_x = d_y = d_{x\&y} = 5$ mm, square hole size: $a = h = 2.5$ mm, and screen thickness $d = 1.25$ mm.

falls further, ε_T^{actual} dives steeply towards around 140% before peaking back up to about 400% again at around 56.5 GHz, the reason for which also as described earlier. Coming now to 120 GHz, it is seen from the inset graph of Fig. 8, which zooms into this frequency, that there is a resonance at this 120 GHz, whose free-space wavenumber $k_0 = 2\pi f\sqrt{(\varepsilon_0\mu_0)} = 2513\,\text{rad/m}$ equals $2(2\pi/d_{x\&y})$ with $d_{x\&y} = 5\,\text{mm}$. This simply exemplifies the situation whereby the k_0-circle passes through the four Floquet nodes at $(m = \pm 2,\ n = 0)$ and $(m = 0,\ n = \pm 2)$, giving rise to surface-wave resonances and thus strong transmission through the hole array, as demonstrated earlier with the dispersion of Fig. 7(a) for the four nodes at $(m = \pm 1,\ n = 0)$ and $(m = 0,\ n = \pm 1)$.

4.2. Oblique Incidence

In addition to the normally incident irradiation of the hole array as discussed in the foregoing subsection, plane waves impinging obliquely and their associated transmission resonance phenomena shall also be herein investigated. Before proceeding, another validation of the present modal method with CST is conveyed in Fig. 9(a) for an obliquely incident TM^z polarized plane wave with $\theta_{inc} = 30°$ and $\phi_{inc} = 45°$ that illuminates a hole array with $d_x = d_y = 5\,\text{mm}$, $a = h = 2.5\,\text{mm}$, and $d = 1.25\,\text{mm}$. Commencing with the present discussions, the oblique incidence angles considered are: $\theta_{inc} = 30°$, $\phi_{inc} = 60°$ and the illuminating radiation is TM^z polarized, thus with the magnetic field having x and y components only. For this case, the zeroth-order power transmission coefficient and transmission efficiency are plotted against frequency in Fig. 9(b) which contains two vertical axes; the left and right ones representing the former and latter, respectively. Evidently, peaks in transmission occur at around 42.5 GHz and 52 GHz. As was for normal incidence, these resonances are due to strong eigen-modal surface-waves propagating along both sides of the perforated screen, which in the same way as before, may be explained by the Floquet nodal graph in conjunction with the modal surface-wave dispersion diagram, as shall in turn be detailed further in the upcoming sub-subsections.

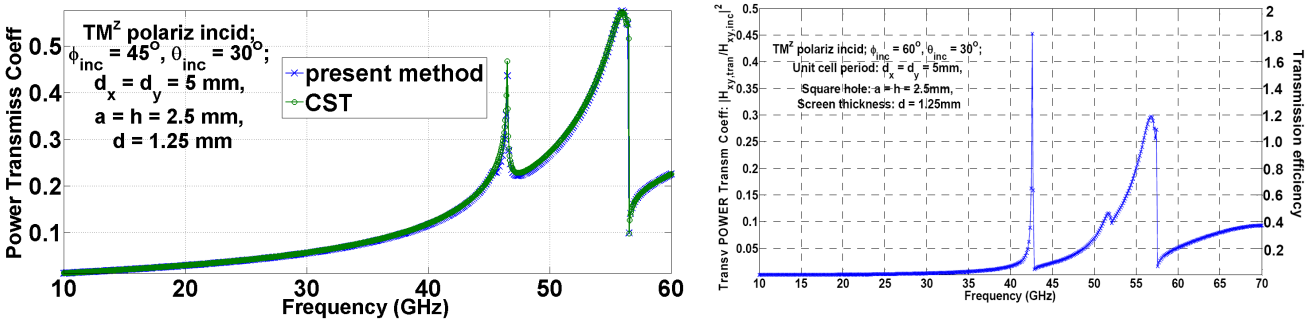

Figure 9. Zeroth-order power transmission coefficient (left vertical axis) and transmission efficiency (right axis) versus frequency for an obliquely incident TM^z polarized plane wave illuminating a square hole array with unit cell period (lattice constant): $d_x = d_y = d_{x\&y} = 5\,\text{mm}$, square hole size: $a = h = 2.5\,\text{mm}$, and screen thickness $d = 1.25\,\text{mm}$, for (a) $\theta_{inc} = 30°$, $\phi_{inc} = 45°$ computed by both the present modal method and CST, and (b) $\theta_{inc} = 30°$, $\phi_{inc} = 60°$ computed by present modal method.

4.2.1. Transmission Peak at 42.5 GHz

Consider the grating lobe diagram in Fig. 10 of which the Floquet nodal lattice is anchored at $(k_{x0} = k_0^\star/4,\ k_{y0} = k_0^\star\sqrt{3}/4)$ associated with $(\theta_{inc} = 30°,\ \phi_{inc} = 60°)$; see (22) and (23), and whereby $k_0^\star$ (free-space wavenumber at $f^\star = 42.789\,\text{GHz} \approx 42.5\,\text{GHz}$) is the radius of the origin-centered circle which intersects the $(m = 0,\ n = -1)$ node. How this $f^\star$ may be acquired is detailed in Appendix B. The surface-wavenumber of the $(m,\ n)$th Floquet harmonic is stated as

$$k_{\rho_{mn}} = \sqrt{k_{x_m}^2 + k_{y_n}^2}, \tag{24}$$

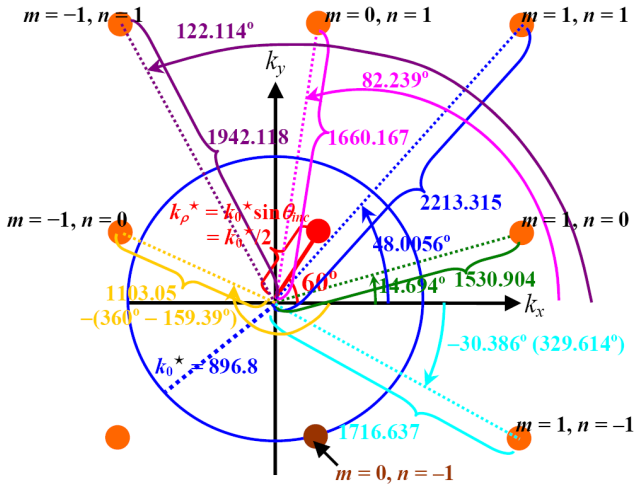

Figure 10. Grating lobe diagram for square cell ($d_{x\&y} = 5\,\text{mm}$) with dominant ($m = n = 0$) Floquet node at ($k_{x0} = k_0^\star/4$, $k_{y0} = k_0^\star\sqrt{3}/4$) corresponding to ($\theta_{inc} = 30°$, $\phi_{inc} = 60°$); see (22) & (23), with $k_0^\star = 896.8\,\text{rad/m}$ (free-space wavenumber at $f^\star = 42.789\,\text{GHz}$) being the radius of circle which intersects the ($m = 0$, $n = -1$) Floquet node. Schematic not drawn to scale.

the specific value of which is indicated by the braces in Fig. 10 for six selected nodes. Each associated azimuth angle, ϕ_{mn}, measured from the k_x axis is given by:

$$\phi_{mn}^{prin} = \tan^{-1}\left|k_{y_n}/k_{x_m}\right| \tag{25a}$$

$$\phi_{mn} = \begin{cases} \phi_{mn}^{prin};\ \text{for } k_{x_m} > 0 \& k_{y_n} > 0 \\ \pi - \phi_{mn}^{prin};\ \text{for } k_{x_m} < 0 \& k_{y_n} > 0 \\ \pi + \phi_{mn}^{prin};\ \text{for } k_{x_m} < 0 \& k_{y_n} < 0 \\ 2\pi - \phi_{mn}^{prin};\ \text{for } k_{x_m} > 0 \& k_{y_n} < 0 \end{cases} \tag{25b}$$

The angles of those aforementioned six selected surface wave-vectors are also annotated in Fig. 10.

Figure 11 presents the dispersion diagrams of TM^z polarized surface waves propagating along various ϕ directions pertaining to different Floquet modes, all for which the grating-lobe lattice is anchored at the dominant ($m = n = 0$) node pertaining to ($\theta_{inc} = \theta_{m=0,n=0} = 30°$, $\phi_{inc} = \phi_{m=0,n=0} = 60°$) and with the k_0 circle intersecting the ($m = 0$, $n = -1$) Floquet node; see Fig. 10. Before proceeding, considering the subtlety here, it is pointed out that this latter zeroth Floquet mode pertains only to the incident wave direction for the illumination scenario of Fig. 9(b) and is not the same as the forcing wavenumber (also bearing the property: $m = n = 0$) entailed in the dispersion generation (resulting in all plots in Fig. 11), which is varied repeatedly over the resonance search domain. Getting back from the brief sidetrack, the dispersion graph for $\phi = \phi_{m=1,n=1} = 48.00564°$ is given in Fig. 11(a), this latter angle constituting the surface-wave propagation direction of the ($m = 1$, $n = 1$) Floquet mode. As observed, a resonant eigen-modal surface wave condition occurs in Fig. 11(a) at the coordinates of ($k_\rho^{reson} \approx 2213.315\,\text{rad/m} = k_{\rho_{m=1,n=1}}$, $f^{reson} \approx 42.789\,\text{GHz} = f^\star$). Hence, at $f^\star = 42.789\,\text{GHz}$ whereby the free-space wavenumber k_0 circle (of radius $k_0^\star = 896.8\,\text{rad/m}$) crosses the ($m = 0$, $n = -1$) Floquet node, as in Fig. 10, the ($m = 1$, $n = 1$) Floquet harmonic is strongly resonant. This $f^\star = 42.789\,\text{GHz}$ concurs closely with the 42.5 GHz at which a transmission resonance is observed in Fig. 9(b), thus being a testament to the notion that surface waves are indeed responsible for the surge in transmission. The coincidence between Floquet modal surface-wave resonances and the transition of the ($m = 0$, $n = -1$) harmonic between the slow (surface) and fast (space) wave regimes is also demonstrative of the effects by branch-point singularities associated with vanishing wavenumber component along the direction perpendicular to the aperture array surface, i.e., the surface wavenumber equals k_0.

What about other Floquet nodes aside from the ($m = 1$, $n = 1$) harmonic, one might ask. Will they also be resonant at $f^\star = 42.789\,\text{GHz}$? The answer is affirmative. Look at the dispersion diagram

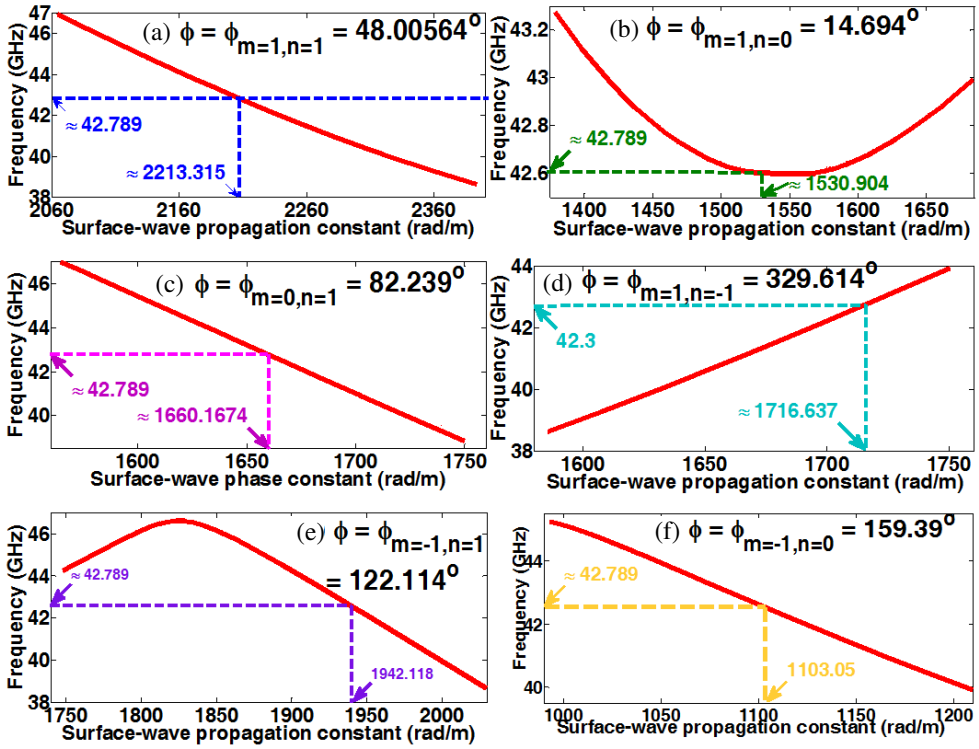

Figure 11. Dispersion diagrams of TM^z polarized surface waves along various ϕ directions pertaining to different Floquet modes, all with grating-lobe lattice anchored at dominant ($m = n = 0$) node associated with ($\theta_{inc} = \theta_{m=0,n=0} = 30°$, $\phi_{inc} = \phi_{m=0,n=0} = 60°$) and with k_0 circle that intersects ($m = 0$, $n = -1$) Floquet node; see Fig. 10. In all plots, the resonant surface wavenumbers k_ρ^{reson} associated with a common $f^{reson} \approx 42.789\,\text{GHz} = f^\star$ are indicated; (a) $\phi = \phi_{m=1,n=1} = 48.00564°$ = surface-wave propagation direction of ($m = 1$, $n = 1$) Floquet mode, with $k_\rho^{reson} \approx 2213.315\,\text{rad/m} = k_{\rho_{m=1,n=1}}$, (b) $\phi = \phi_{m=1,n=0} = 14.694°$, with $k_\rho^{reson} \approx 1530.904\,\text{rad/m} = k_{\rho_{m=1,n=0}}$, (c) $\phi = \phi_{m=0,n=1} = 82.239°$, with $k_\rho^{reson} \approx 1660.1674\,\text{rad/m} = k_{\rho_{m=0,n=1}}$, (d) $\phi = \phi_{m=1,n=-1} = 329.614°$ with $k_\rho^{reson} \approx 1716.637\,\text{rad/m} = k_{\rho_{m=1,n=-1}}$, (e) $\phi = \phi_{m=-1,n=1} = 122.114°$ with $k_\rho^{reson} \approx 1942.118\,\text{rad/m} = k_{\rho_{m=-1,n=1}}$, and (f) $\phi = \phi_{m=-1,n=0} = 159.39°$ with $k_\rho^{reson} \approx 1103.05\,\text{rad/m} = k_{\rho_{m=-1,n=0}}$.

in Fig. 11(b), also for TM^z polarization but this time for $\phi = \phi_{m=1,n=0} = 14.694°$ instead, being the surface-propagation direction of the ($m = 1$, $n = 0$) mode. A resonance point with coordinates: ($k_\rho^{reson} \approx 1530.904\,\text{rad/m} = k_{\rho_{m=1,n=0}}$, $f^{reson} \approx 42.789\,\text{GHz} = f^\star$) is identified, which tallies back once more with Fig. 10, thereby further substantiating the concept of ascribing surface-wave resonances to the occurrences of Floquet harmonics along the periphery separating the fast and slow wave regimes.

More fortification of this perspective is given by the dispersion graphs of Figs. 11(c) through 11(f) for $\phi = \phi_{m=0,n=1} = 82.239°$, $\phi = \phi_{m=1,n=-1} = 329.614°$, and $\phi = \phi_{m=-1,n=1} = 112.114°$ pertaining respectively to the ($m = 0$, $n = 1$), ($m = 1$, $n = -1$), ($m = -1$, $n = 1$), and ($m = -1$, $n = 0$) Floquet harmonics of Fig. 10. At $f^\star = 42.789\,\text{GHz}$, the associated resonant surface wavenumbers as indicated in all these three dispersion diagrams indeed tally up with those of the three aforementioned Floquet harmonics as displayed in Fig. 10.

4.2.2. Transmission Peak at 52 GHz

The same foregoing reasons for the surge in transmission at around 42.5 GHz reapply to the one at 52 GHz (see Fig. 9(b) again). This time, the accountable surface wave resonances are tied instead with the ($m = -1$, $n = 0$) Floquet mode attaining a wavenumber at $f^\star = 52.075\,\text{GHz}$ which equals that of propagating plane-waves in free-space, $k_0^\star = 1091.41\,\text{rad/m}$; the associated grazing wave thus sitting

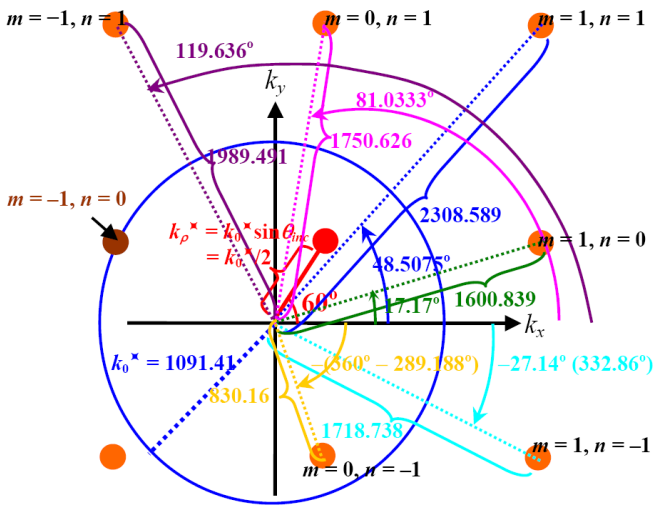

Figure 12. Grating lobe diagram for square cell ($d_{x\&y} = 5\,\text{mm}$) with dominant ($m = n = 0$) Floquet node at ($k_{x0} = k_0^\star/4$, $k_{y0} = k_0^\star\sqrt{3}/4$) corresponding to ($\theta_{inc} = 30°$, $\phi_{inc} = 60°$); see (22) & (23), with $k_0^\star = 1091.41\,\text{rad/m}$ (free-space wavenumber at $f^\star = 52.075\,\text{GHz}$) being the radius of circle which intersects the ($m = -1$, $n = 0$) Floquet node. Schematic not drawn to scale.

right on the borderline between being regarded as a fast space wave and a slow surface wave. This is illustrated in Fig. 12, in which the surface wavenumbers, $k_{\rho_{mn}}$, of various (m, n) Floquet modes and their associated azimuth angles of propagation, ϕ_{mn}, are also indicated according to (24) and (25b). As before, the Floquet lattice is anchored at the dominant ($m = 0$, $n = 0$) node pertaining to ($\theta_{inc} = \theta_{m=0,n=0} = 30°$, $\phi_{inc} = \phi_{m=0,n=0} = 60°$). Again, refer to Appendix B for the details on how $f^\star$ is obtained.

Dispersion diagrams for azimuth angles of surface-wave propagation that take on the same ϕ directions as those of likewise six selected Floquet nodes are presented in Figs. 13(a) through 13(f), in each of which the resonant surface-wavenumber corresponding to a universal frequency $f^\star = 52.075\,\text{GHz}$ is indicated. Clearly, all aforementioned associated eigen-modal surface wavenumbers tally up well with the indicated $k_{\rho_{mn}}$ values in Fig. 12, thus once more corroborating the theorized mechanism responsible for transmission resonances.

4.2.3. Intersection of k_0 Circle with Other Floquet Nodes — Account for Other Transmission Peaks

Consider now, a periodically arranged lattice of nodes in the Floquet lattice (grating lobe) diagram, with adjacent nodes being separated by $2\pi/d_x$ and $2\pi/d_x$ along the k_x and k_y axes, respectively. The $(m = 0,\ n = 0)^{th}$ node of this lattice is anchored at coordinates ($k_x = k_{x0}$, $k_y = k_{y0}$), these k_{x0} and k_{y0} being acquired from (29), which in the present context are with $\theta_{inc} = 30°$, $\phi_{inc} = 60°$ and for a square cell of periods $d_x = d_y = d_{x\&y} = 5\,\text{mm}$. At this point, however, the free-space wavenumber, $k_0 = 2\pi f\sqrt{(\varepsilon_0\mu_0)}$ which exists as a term in the expressions for both k_{x0} and k_{y0} in (29) has not yet been specified. The k_0 values of interest herein are those pertaining to so-called k_0-circles (having radii k_0 and centered at the origin of the k_x-k_y lattice diagram) that intersect various prescribed $(m,\ n)^{th}$ Floquet nodes. The frequency f whose k_0-circle intersects any certain $(m,\ n)^{th}$ node may be calculated according to the details of Appendix B.

Doing so, Table 1 tabulates, in ascending order, these aforesaid frequencies and their associated Floquet modal indices, m and n, of the lattice nodes through which the k_0-circles of those latter frequencies cut. The first two frequencies: 42.789 GHz and 52.075 GHz, are those that have already been discussed (in subsections *a* and *b*). Not surprisingly, the third frequency in the table: 57.505 GHz, corresponds indeed to the third summit in Fig. 9(b). The remaining three frequencies on the list, namely 84.368 GHz, 85.578 GHz, and 89.461 GHz, all tally up well with the peaks in Fig. 14, being the same graph as Fig. 9(b) but for frequencies from 82.5 GHz to 90 GHz, a window higher up in the spectrum.

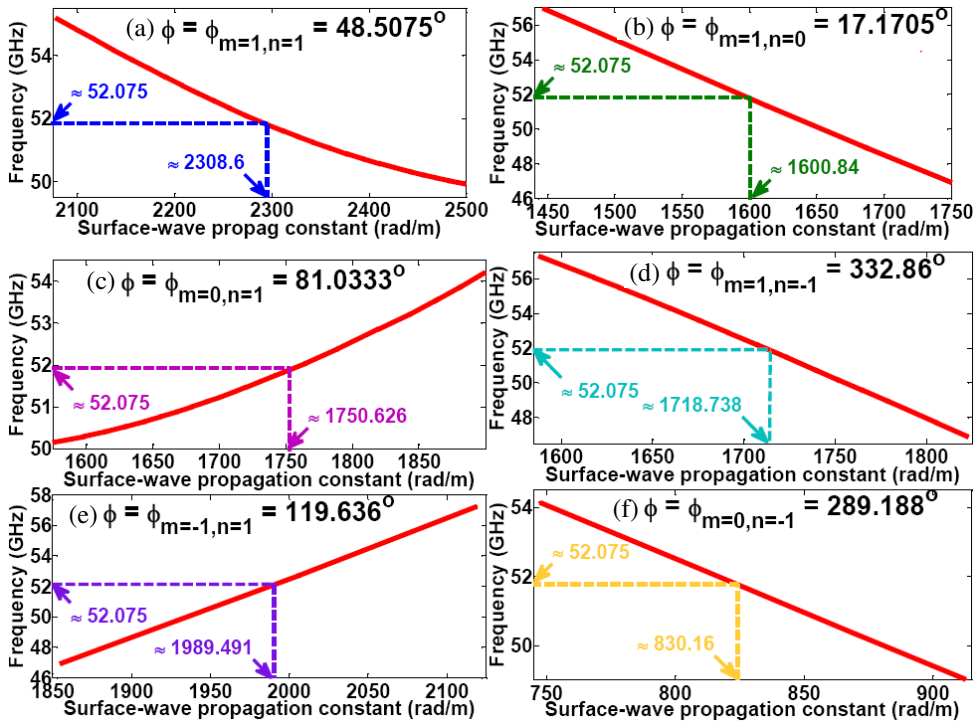

Figure 13. Dispersion diagrams of TM^z polarized surface waves along various ϕ directions pertaining to different Floquet modes, all with grating-lobe lattice anchored at dominant ($m = n = 0$) node associated with ($\theta_{inc} = \theta_{m=0,n=0} = 30°$, $\phi_{inc} = \phi_{m=0,n=0} = 60°$) and with k_0 circle that intersects ($m = -1$, $n = 0$) Floquet node; see Fig. 12. In all plots, the resonant surface wavenumbers k_ρ^{reson} associated with a common $f^{reson} \approx 52.075\,\text{GHz} = f^\star$ are indicated; (a) $\phi = \phi_{m=1,n=1} = 48.5075° =$ surface-wave propagation direction of ($m = 1$, $n = 1$) Floquet mode, with $k_\rho^{reson} \approx 2308.589\,\text{rad/m} = k_{\rho_{m=1,n=1}}$, (b) $\phi = \phi_{m=1,n=0} = 17.1705°$, with $k_\rho^{reson} \approx 1600.839\,\text{rad/m} = k_{\rho_{m=1,n=0}}$, (c) $\phi = \phi_{m=0,n=1} = 81.0333°$, with $k_\rho^{reson} \approx 1750.626\,\text{rad/m} = k_{\rho_{m=0,n=1}}$, (d) $\phi = \phi_{m=1,n=-1} = 332.86°$ with $k_\rho^{reson} \approx 1718.738\,\text{rad/m} = k_{\rho_{m=1,n=-1}}$, (e) $\phi = \phi_{m=-1,n=1} = 119.636°$ with $k_\rho^{reson} \approx 1989.491\,\text{rad/m} = k_{\rho_{m=-1,n=1}}$, and (f) $\phi = \phi_{m=0,n=-1} = 289.188°$ with $k_\rho^{reson} \approx 830.16\,\text{rad/m} = k_{\rho_{m=0,n=-1}}$.

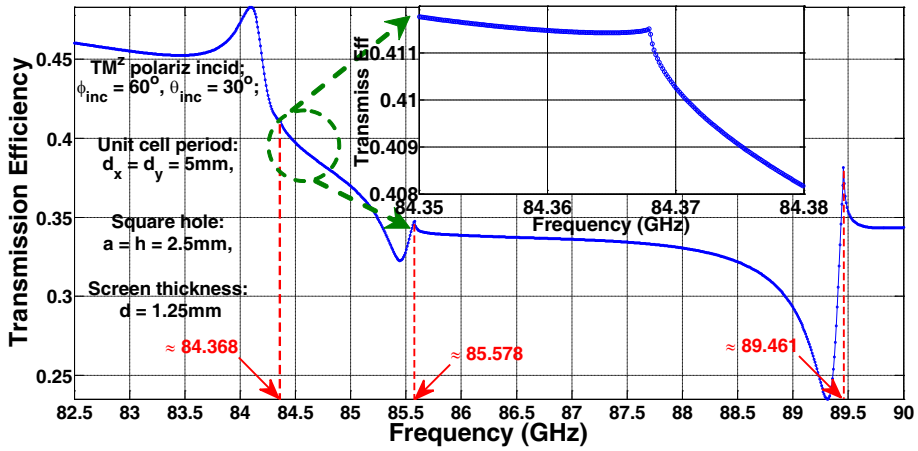

Figure 14. Same as Fig. 9(b), but higher up in the spectrum.

Table 1. Frequencies of free-space wavenumber-circles intersecting various floquet modal indices: for $\theta_{inc} = 30°$, $\phi_{inc} = 60°$ and square cell of lattice constant 5 mm (Method detailed in Appendix B).

Frequency (GHz)	m	n
42.789	0	-1
52.075	-1	0
57.505	-1	-1
84.368	1	-1
85.578	0	-2
89.461	-1	-2

5. COMPLEMENTARY ARRAY OF CONDUCTING RECTANGULAR PLATES BY BABINET'S PRINCIPLE

With the modal treatment of plane-wave scattering by a rectangular hole array presented herein, the corresponding solution for the complementary structure constituting an array of conducting rectangular plates may also be acquired using Babinet's principle [55]. This theorem is stated as follows. Consider an unobstructed plane wave that illuminates, under separate scenarios, both a thin perforated conducting screen and its complementary array of thin conducting plates having the same shape and size as the holes of the former as well as a shared periodicity. Observed at a location on the output (transmission) side of both periodic structures, the fields of that excitation plane wave in the absence of both obstructers shall then be equal to the sum of the transmitted fields, at that same spot, that are scattered by both dual arrays (i.e., under the presence of each dual scenario independently). For the same electric current excitation source on the input side and the same ambient homogeneous medium, the plates shall become magnetic conducting when they complement holes cut out of an electric conducting screen.

Using this concept, the transmission of a normally incident plane wave (TE^z polarization, $\phi_{inc} = \theta_{inc} = 0$) through an array of thin magnetic conducting square plates (3 mm by 3 mm) with thickness $d = 0.01$ mm and periods $d_x = d_y = 5$ mm, all immersed in vacuum, is computed over a span of frequencies using the field solutions, from the present modal method, for the complementary electric conducting perforated screen also in free space and illuminated by that same plane wave excitation. The graph of this aforementioned transmission versus frequency is plotted in Fig. 15 as cross markers. Interposed within this same graph is the trace of circle markers for the dual array of magnetic conducting square plates also placed in vacuum, but this time simulated directly by CST. As seen, good congruence

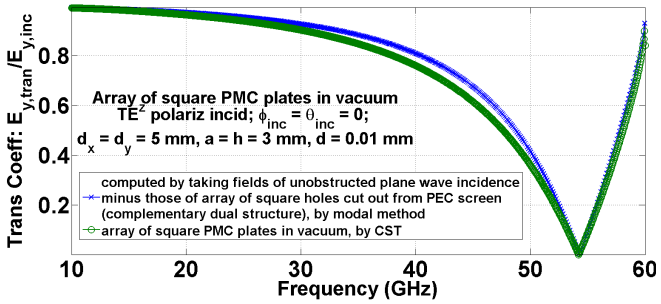

Figure 15. Transmission spectrum of normally-incident plane wave (TE^z polarization, $\phi_{inc} = \theta_{inc} = 0$) through an array of thin magnetic conducting square plates (3 mm by 3 mm) with thickness $d = 0.01$ mm and periods $d_x = d_y = 5$ mm, all immersed in vacuum, computed using the field solutions, from present modal method, of the complementary electric conducting perforated screen also in free space and illuminated by that same plane wave excitation, given by cross markers. Circle markers represent corresponding trace for the dual array of magnetic conducting square plates also placed in vacuum, but this time simulated directly by CST.

between both dual scenarios is achieved, thereby demonstrating the ability of the present modal approach in also treating the plane-wave scattering by complementary arrays of conducting plates.

6. CONCLUSIONS

A rigorous full-wave modal analysis of penetrable rectangular hole arrays pierced through a planar conducting screen of finite thickness has been presented. Based on the method of moments, Green's functions for rectangular cavities and planar multilayer structures are used, those for the latter being in the spectral domain. Floquet theorem is also thus employed. This addresses, to an extent, the lack or absence of detailed treatment approaches of such a structure in the literature.

With the numerical tool developed based on this modal formulation, computed results in the forms of transmission spectra (graphs of transmission versus frequency), modal surface wave dispersion diagrams, and field distributions can all be generated. It has been demonstrated how the Floquet nodal lattice diagram (or grating lobe diagram in array theory) and the surface-wave dispersion diagram can be tied up coherently with the locations of peaks observed in the transmission spectrum. As such, surges in wave penetration through the perforated screen can be appreciated as being due to modal surface-wave resonances, recognized also as surface-plasmon polaritons (SPP) that are set off by the periodically-textured conducting surface. Such enhanced energy diffusion occurs even at frequencies where each hole is considerably less than the wavelength of the irradiation, in violation of classical aperture theory which predicts the inability of electrically small holes in allowing electromagnetic fields and waves to pass through them, resulting in so-called extraordinary transmission.

Oblique incidences with consideration of the polarization of the arriving plane wave have also been taken into account in this work. This is an element that could be absent elsewhere in the literature.

It is hoped that the materials presented in this work could strengthen the appreciation of the mechanisms behind extraordinary transmission through subwavelength hole arrays, or at least offer alternative insights into them. It is also intended to trigger new ideas for continued research in this exciting and growing subject that lends itself to a vast range of applications in forefront topics in science and technology.

ACKNOWLEDGMENT

This work was partially supported by the "Center for mmWave Smart Radar Systems and Technologies" under the Featured Areas Research Center Program within the framework of the Higher Education Sprout Project by the Ministry of Education (MOE), and partially supported under MOST 107-3017-F-009-001, in Taiwan.

APPENDIX A. EXPLICIT ORTHONORMALIZED RECTANGULAR WAVEGUIDE MODAL FIELD FUNCTIONS

The transverse waveguide modal field functions entailed throughout this paper must be in their orthonormalized forms, as required by the dyadic cavity Green's functions. For a coordinate-origin centered rectangular waveguide with width and height along x and y being a and h respectively, and homogeneously filled with a medium of parameters (μ_{cav}, ε_{cav}), the following are stated.

$$\bar{e}^{cav}_{t_{pqTE}}(x,y) = \begin{cases} \hat{x}\sqrt{\dfrac{2Z^{TE}_{0q}}{ah}}S_y & p=0, q\neq 0 \\ -\hat{y}\sqrt{\dfrac{2Z^{TE}_{p0}}{ah}}S_x & p\neq 0, q=0 \\ \dfrac{2}{k^{cav}_{c_{pq}}}\sqrt{\dfrac{Z^{TE}_{pq}}{ah}}\left(\hat{x}k_{y_q}C_xS_y - \hat{y}k_{x_p}S_xC_y\right) & p\neq 0, q\neq 0 \end{cases}$$

$$\vec{h}^{cav}_{t_{pqTE}(x,y)} = \begin{cases} \hat{y}\sqrt{\dfrac{2Y^{TE}_{0q}}{ah}}\,[S_y] & p=0, q\neq 0 \\ \hat{x}\sqrt{\dfrac{2Y^{TE}_{p0}}{ah}}\,[S_x] & p\neq 0, q=0 \\ \dfrac{2}{k^{cav}_{c_{pq}}}\sqrt{\dfrac{Y^{TE}_{pq}}{ah}}\left(\hat{x}k_{x_p}S_xC_y+\hat{y}k_{y_q}C_xS_y\right) & p\neq 0, q\neq 0 \end{cases}$$

$$\vec{e}^{cav}_{t_{pqTM}(x,y)} = -\frac{2}{k^{cav}_{c_{pq}}}\sqrt{\frac{Z^{TM}_{pq}}{ah}}\left(\hat{x}k_{x_p}C_xS_y+\hat{y}k_{y_q}S_xC_y\right),$$

$$\vec{h}^{cav}_{t_{pqTM}}(x,y) = \frac{2}{k^{cav}_{c_{pq}}}\sqrt{\frac{Y^{TM}_{pq}}{ah}}\left(\hat{x}k_{y_q}S_xC_y-\hat{y}k_{x_p}C_xS_y\right)$$

where $k_{x_p} = p\pi/a$; $k_{y_q} = q\pi/h$; $k^{cav}_{c_{pq}} = \sqrt{k^2_{x_p}+k^2_{y_q}}$, $\begin{Bmatrix} C_x \\ S_x \end{Bmatrix} = \begin{Bmatrix} \cos \\ \sin \end{Bmatrix}\left(k_{x_p}x+\frac{p\pi}{2}\right)$; $\begin{Bmatrix} C_y \\ S_y \end{Bmatrix} = \begin{Bmatrix} \cos \\ \sin \end{Bmatrix}\left(k_{y_q}y+\frac{q\pi}{2}\right)$, $Z^{TE}_{pq} = j\omega\mu_{cav}\Big/\gamma^{cav}_{z_{pq}} = \left(Y^{TE}_{pq}\right)^{-1}$; $Z^{TM}_{pq} = \gamma^{cav}_{z_{pq}}\Big/j\omega\varepsilon_{cav} = \left(Y^{TM}_{pq}\right)^{-1}$, $\gamma^{cav}_{z_{pq}} = \sqrt{\left(k^{cav}_{c_{pq}}\right)^2-k^2_{cav}}$, $k_{cav} = \omega\sqrt{\mu_{cav}\varepsilon_{cav}}$.

In this way, the following orthonormality property holds:

$$\int_{y=-h/2}^{y=h/2}\int_{x=-a/2}^{x=a/2}\left(\vec{e}^{cav}_{t_{pqr}}\times\vec{h}^{cav}_{t_{uvw}}\right)\cdot\hat{z}dxdy = \delta_{pqr,uvw} = \begin{cases} 1, \text{ if } p=u, q=v, r\equiv w \\ 0, \text{ otherwise} \end{cases}$$

APPENDIX B. DETERMINATION OF FREQUENCY WHOSE WAVENUMBER CIRCLE IN GRATING-LOBE DIAGRAM INTERSECTS ANY FLOQUET MODAL NODE

This Appendix seeks to determine the frequency whose k_0 wavenumber circle in the k_x-k_y grating lobe diagram intersects any specified pair of (m, n) Floquet modal indices of a grating-lobe lattice anchored at (k_{x0}, k_{y0}) subjected to specified ($\theta_{00}=\theta_{inc}$, $\phi_{00}=\phi_{inc}$).

From the basics of Eqs. (24) and (25b), the azimuthal surface-wavenumber, $k_{\rho_{mn}}$, for the (m, n)th Floquet mode to be intersected is then equated to k_0:

$$k_{\rho_{mn}} = k_0 \Rightarrow \sqrt{\left[\left(k_0\sin\theta_{00}\cos\phi_{00}+2m\pi/d_x\right)^2+\left(k_0\sin\theta_{00}\sin\phi_{00}+2n\pi/d_y\right)^2\right]} = k_0 \tag{B1}$$

leading to:

$$\left(\cos^2\theta_{00}\right)k_0^2 - 4\pi\sin\theta_{00}\left(\frac{m\cos\phi_{00}}{d_x}+\frac{n\sin\phi_{00}}{d_y}\right)k_0 - 4\pi^2\left(\frac{m^2}{d_x^2}+\frac{n^2}{d_y^2}\right) = 0 \tag{B2}$$

being a quadratic equation which can then be solved for f:

$$f = \frac{\sin\theta_{00}\left(\dfrac{m\cos\phi_{00}}{d_x}+\dfrac{n\sin\phi_{00}}{d_y}\right)\pm\sqrt{\sin^2\theta_{00}\left(\dfrac{m\cos\phi_{00}}{d_x}+\dfrac{n\sin\phi_{00}}{d_y}\right)^2+\cos^2\theta_{00}\left(\dfrac{m^2}{d_x^2}+\dfrac{n^2}{d_y^2}\right)}}{\cos^2\theta_{00}\sqrt{\mu_0\varepsilon_0}} \tag{B3}$$

REFERENCES

1. Renk, K. F. and L. Genzel, "Interference filters and Fabry-Perot interferometers for the far infrared," *Appl. Opt.*, Vol. 1, No. 5, 643–648, Sep. 1962.
2. Ulrich, R., "Far-infrared properties of metallic mesh and its complementary structure," *Infrared Phys.*, Vol. 7, No. 1, 37–55, Mar. 1967.
3. Ressler, G. M. and K. D. Moller, "Far infrared bandpass filters and measurements on a reciprocal grid," *Appl. Opt.*, Vol. 6, No. 5, 893–896, May 1967.
4. Mitsuishi, A., Y. Otsuka, S. Fujita, and H. Yoshinaga, "Metal mesh filters in the far infrared region," *Jpn. J. Appl. Phys.*, Vol. 2, No. 9, 574–577, Sep. 1963.
5. Chen, C. C., "Diffraction of electromagnetic waves by a conducting screen perforated periodically with circular holes," *IEEE Trans. Microw. Theory Tech.*, Vol. 19, No. 5, 475–481, May 1971.
6. Chen, C. C., "Transmission through a conducting screen perforated periodically with apertures," *IEEE Trans. Microw. Theory Tech.*, Vol. 18, No. 9, 627–632, Sep. 1970.
7. Lee, S. W., G. Zarrillo, and C. L. Law, "Simple formulas for transmission through periodic metal grids or plates," *IEEE Trans. Antennas Propag.*, Vol. 30, No. 5, 904–909, Sep. 1982.
8. Ebbesen, T. W., H. J. Lezec, H. F. Ghaemi, T. Thio, and P. A. Wolff, "Extraordinary optical transmission through sub-wavelength hole arrays," *Nature*, Vol. 391, 667–669, London, Feb. 1998.
9. Bethe, H. A., "Theory of diffraction by small holes," *Phys. Rev.*, Vol. 66, Nos. 7 & 8, 163–182, Oct. 1944.
10. Sambles, J. R., "More than transparent," *Nature*, Vol. 391, No. 6668, 641–642, London, Feb. 1998.
11. Thio, T., H. J. Lezec, and T. W. Ebbesen, "Strongly enhanced optical transmission through subwavelength holes in metal films," *Physica B*, Vol. 279, 90–93, Amsterdam, 2000.
12. Gordon, R., A. G. Brolo, D. Sinton, and K. L. Kavanagh, "Resonant optical transmission through hole-arrays in metal films: physics and applications," *Laser & Photon. Rev.*, Vol. 4, No. 2, 311–335, Feb. 2010.
13. Genet, C. and T. W. Ebbesen, "Light in tiny holes," *Nature*, Vol. 445, 39–46, Jan. 2007.
14. Coe, J. V., J. M. Heer, S. Teeters-Kennedy, H. Tian, and K. R. Rodriguez, "Extraordinary transmission of metal films with arrays of subwavelength holes," *Ann. Rev. Phys. Chem.*, Vol. 59, 179–202, 2008.
15. Stewart, M. E., C. R. Anderton, L. B. Thompson, J. Maria, S. K. Gray, J. A. Rogers, and R. G. Nuzzo, "Nanostructured plasmonic sensors," *Chem. Rev.*, Vol. 108, 494–521, Jan. 2008.
16. Gordon, R., D. Sinton, K. L. Kavanagh, and A. G. Brolo, "A new generation of sensors based on extraordinary optical transmission," *Acc. Chem. Res.*, Vol. 41, No. 8, 1049–1057, Jul. 2008.
17. Raether, H., *Surface Plasmons on Smooth and Rough Surfaces and on Gratings*, Springer-Verlag, Berlin, 1988.
18. Ghaemi, H. F., T. Thio, D. E. Grupp, T. W. Ebbesen, and H. J. Lezec, "Surface plasmons enhance optical transmission through subwavelength holes," *Phy. Rev. B*, Vol. 58, 6779–6782, Sep. 1998.
19. Grupp, D. E., H. J. Lezec, T. W. Ebbesen, K. M. Pellerin, and T. Thio, "Crucial role of metal surface in enhanced transmission through subwavelength apertures," *Appl. Phys. Lett.*, Vol. 77, 1569–1571, 2000.
20. Schroter, U. and D. Heitmann, "Surface-plasmon-enhanced transmission through metallic gratings," *Phys. Rev. B*, Vol. 58, No. 23, 419–421, Dec. 1998.
21. Treacy, M. M. J., "Dynamical diffraction in metallic optical gratings," *Appl. Phys. Lett.*, Vol. 75, No. 5, 606–608, Aug. 1999.
22. Porto, J. A., F. J. Garcia-Vidal, and J. B. Pendry, "Transmission resonances on metallic gratings with very narrow slits," *Phys. Rev. Lett.*, Vol. 83, No. 14, 2845–2848, Oct. 1999.
23. Popov, E., M. Neviere, S. Enoch, and R. Reinisch, "Theory of light transmission through subwavelength periodic hole arrays," *Phys. Rev. B*, Vol. 62, No. 23, 16100–16108, Dec. 2000.
24. Enoch, S.. E. Popov, M. Neviere, R. Reinisch, "Enhanced light transmission by hole arrays," *J. Opt. A*, Vol. 4, No. 5, S83–S87, Aug. 2002.

25. Krishan, A., T. Thio, T. J. Kim, H. J. Lezec, T. W. Ebbesen, P. A. Wolff, J. B. Pendry, L. Martin-Moreno, and F. J. Garcia-Vidal, "Evanescently coupled resonance in surface plasmon enhanced transmission," *Opt. Commun.*, Vol. 200, Nos. 1–6, 1–7, Dec. 2001.
26. Martin-Moreno, L., F. J. Garcia-Vidal, H. J. Lezec, K. M. Pellerin, T. Thio, J. B. Pendry, and T. W. Ebbesen, "Theory of extraordinary optical transmission through subwavelength hole arrays," *Phys. Rev. Lett.*, Vol. 86, 1114–1117, Feb. 2001.
27. Darmanyan, S. A., A. V. Zayats, "Light tunneling via resonant surface plasmon polariton states and the enhanced transmission of periodically nanostructured metal films: an analytical study," *Phys. Rev. B*, Vol. 67, 035424, 1–7, Jan. 2003.
28. Popov, E., M. Neviere, P. Boyer, and N. Bonod, "Light transmission through a subwavelength hole," *Optics Commun.*, Vol. 255, 338–348, Jun. 2005.
29. Sobnack, M. B., W. C. Tan, N. P. Wanstall, T. W. Preist, and J. R. Sambles, "Stationary surface plasmons on a zero-order metal grating," *Phys. Rev. Lett.*, Vol. 80, No. 25, 5667–5670, Jun. 1998.
30. Astilean, S., P. Lalanne, and M. Palamaru, "Light transmission through metallic channels much smaller than the wavelength," *Opt. Commun.*, Vol. 175, 265–273, Mar. 2000.
31. Takakura, Y., "Optical resonance in a narrow slit in a thick metallic screen," *Phys. Rev. Lett.*, Vol. 86, No. 24, 5601–5603, Jun. 2001.
32. Krishnan, A., T. Thio, T. J. Kim, H. J. Lezec, T. W. Ebbesen, P. A. Wolff, J. Pendry, L. Martin-Moreno, and F. J. Garcia-Vidal, "Evanescently coupled resonance in surface plasmon enhanced transmission," *Optics Commun.*, Vol. 200, 1–7, Dec. 2001.
33. Medina, F., F. Mesa, and R. Marques, "Extraordinary transmission through arrays of electrically small holes from a circuit theory perspective," *IEEE Trans. Microw. Theory Techn.*, Vol. 56, No. 2, 3108–3120, Dec. 2008.
34. Medina, F., F. Mesa, and D. C. Skigin, "Extraordinary transmission through arrays of slits: a circuit theory model," *IEEE Trans. Microw. Theory Techn.*, Vol. 58, No. 1, 105–115, Jan. 2010.
35. Beruete, M., M. Navarro-Cia, and M. S. Ayza, "Understanding anomalous extraordinary transmission from equivalent circuit and grounded slab concepts," *IEEE Trans. Microw. Theory Techn.*, Vol. 59, No. 9, 2180–2188, Sep. 2011.
36. Beruete, M., I. Campillo, M. Navarro-Cía, F. Falcone, and M. Sorolla, "Molding left- or right-handed metamaterials by stacked cutoff metallic hole arrays," *IEEE Trans. Antennas Propag.*, Vol. 55, No. 6, 1514–1521, Jun. 2007.
37. Delgado, V., R. Marques, and L. Jelinek, "Coupled-wave surface-impedance analysis of extraordinary transmission through single and stacked metallic screens," *IEEE Trans. Antennas Propag.*, Vol. 61, No. 3, 1342–1351, Mar. 2013.
38. Beruete, M., M. Sorolla, I. Campillo, and J. S. Dolado, "Increase of the transmission in cut-off metallic hole arrays," *IEEE Microw. Wireless Comp. Lett.*, Vol. 15, No. 2, 116–118, Feb. 2005.
39. Lomakin, V. and E. Michielssen, "Enhanced transmission through metallic plates perforated by arrays of subwavelength holes and sandwiched between dielectric slabs," *Phys. Rev. B*, Vol. 71, No. 23, 235117, Jun. 2005.
40. Lomakin, V. and E. Michielssen, "Transmission of transient plane waves through perfect electrically conducting plates perforated by periodic arrays of subwavelength holes," *IEEE Trans. Antennas Propag.*, Vol. 54, No. 3, 970–984, Mar. 2006.
41. Bravo-Abad, J., I. Martin-Moreno, and F. J. Garcia-Vidal, "Resonant transmission of light through subwavelength holes in thick metal films," *IEEE J. Selec. Topics Quan. Electron.*, Vol. 12, No. 6, 1221–1227, Nov./Dec. 2006.
42. Mary, A., S. Rodrigo, L. Martín-Moreno, and F. García-Vidal, "Theory of light transmission through an array of rectangular holes," *Phys. Rev. B*, Vol. 76, No. 19, 195414, Nov. 2007.
43. Chen, Y., Y. Wang, Y. Zhang and S. Liu, "Numerical investigation of the transmission enhancement through subwavelength hole array," *Optics Commun.*, Vol. 274, 236–240, Feb. 2007.
44. Schuchinsky, A. G., D. E. Zelenchuk, and A. M. Lerer, "Enhanced transmission in microwave arrays of periodic sub-wavelength apertures," *J. Opt. A: Pure Appl. Opt.*, Vol. 7, S102–S109, Jan. 2005.

45. Schuchinsky, A. G., D. E. Zelenchuk, A. M. Lerer, and R. Dickie, "Full-wave analysis of layered aperture arrays," *IEEE Trans. Antennas Propag.*, Vol. 54, No. 2, 490–502, Feb. 2006.
46. Monni, S., G. Gerini, A. Neto, and A. G. Tijhuis, "Multi-mode equivalent networks for the design and analysis of frequency selective surfaces," *IEEE Trans. Antennas Propag.*, Vol. 55, No. 10, 2824–2835, Oct. 2007.
47. Beruete, M., M. Sorolla, I. Campillo, J. S. Dolado, L. Martín-Moreno, J. Bravo-Abad, and F. J. García-Vidal, "Enhanced millimeter-wave transmission through subwavelength hole arrays," *Opt. Lett.*, Vol. 29, No. 21, 2500–2502, Nov. 2004.
48. Beruete, M., M. Sorolla, I. Campillo, J. S. Dolado, L. Martín-Moreno, J. Bravo-Abad, and F. J. García-Vidal, "Enhanced millimeter wave transmission through quasioptical subwavelength perforated plates," *IEEE Trans. Antennas Propag.*, Vol. 53, No. 6, 1897–1903, Jun. 2005.
49. Hu, D. and Y. Zhang, "Localized surface plasmons-based transmission enhancement of terahertz radiation through metal aperture arrays," *Optik*, Vol. 121, 1423–1426, Feb. 2009.
50. Shirmanesh, G. K., A. Khavasi, and K. Mehrany, "Accurate effective medium theory for arrays of metallic nanowires," *Journal of Optics*, Vol. 17, 025104, 2015.
51. Yarmoghaddam, E., G. K. Shirmanesh, A. Khavasi, and K. Mehrany, "Circuit model for periodic array of slits with multiple propagating diffracted orders," *IEEE Trans. Antennas Propag.*, Vol. 62, No. 8, 4041–4048, Aug. 2018.
52. Ng Mou Kehn, M., "Modal analysis of substrate integrated waveguides with rectangular via-holes using cavity and multilayer Green's functions," *IEEE Trans. Microw. Theory Techn.*, Vol. 62, No. 10, 2214–2231, Oct. 2014.
53. Lord Rayleigh, "On the dynamical theory of gratings," *Proc. R. Soc. London*, Ser. A, Vol. 79, 399, 1907.
54. Lord Rayleigh, "Note on the remarkable case of diffraction spectra described by Prof. Wood," *Philos. Mag.*, Vol. 14, 60, 1907.
55. Balanis, C. A., *Antenna Theory, Analysis and Design*, 2nd Edition, John Wiley & Sons, Inc., 1997.